



RESEARCH

Nonlinear mirrored-stiffness design method for quasi-zero stiffness vibration isolators

Minghao Wang · Ruilan Tian · Xiaolong Zhang · Shen Li · Qiubao Wang

Received: 6 May 2024 / Accepted: 7 July 2024 / Published online: 15 July 2024
© The Author(s), under exclusive licence to Springer Nature B.V. 2024

Abstract The phenomenon of stiffness hardening has detrimental influence on the natural frequency and the width of vibration isolation frequency bands, which significantly confines the development of quasi-zero-stiffness vibration isolators (QZSVIs). To overcome this restriction, the nonlinear mirrored-stiffness design method (NMSM) is proposed and its applicable condition is revealed. Based on the mechanism of stiffness hardening, a nonlinear spring (NS) is designed by the NMSM. NS possesses nonlinear restoring force and a mirror-image relationship with the targeted negatives stiffness. The mathematical model of the NS is established based on Heaviside function. Coupled QZSVIs (CQZSVIs) are constructed by a concave metastructure with multiple stiffness properties and the NS to validate the NMSM. A prototype of the CQZSVI is fabricated to prove the correctness of the theoretical analysis. The practical tests of the CQZSVI demonstrate an obvious QZS

region where the restoring force remains approximately constant and the stiffness is almost invariable and close to zero. The results of sweep-frequency experiments show that the CQZSVI has a natural frequency of about 0.8 Hz and a broad effective vibration isolation region starting from about 1.1 Hz. Its transmissibility is about -15 dB at 3 Hz and is about -20 dB at 3.5 Hz. The NMSM successfully breaks through the bottleneck of the development of QZSVIs and produces a new approach for the construction of low-frequency vibration isolators.

Keywords Quasi-zero stiffness · Low-frequency vibration isolation · Stiffness compensation · Nonlinear vibration · Nonlinear spring

Abbreviations

QZSVI	Quasi-zero stiffness vibration isolator
QZS	Quasi-zero-stiffness
SD	Smooth and discontinuous
XSS	X-shaped structure
NMSM	Nonlinear mirrored-stiffness design method
NS	Nonlinear spring
CQZSVI	Coupled quasi-zero-stiffness vibration isolator

M. Wang · R. Tian (✉) · X. Zhang · S. Li · Q. Wang
Hebei Research Center of the Basic Discipline
Engineering Mechanics, Shijiazhuang Tiedao University,
Shijiazhuang 050043, China
e-mail: tianrl@stdu.edu.cn

M. Wang
School of Traffic and Transportation, Shijiazhuang Tiedao
University, Shijiazhuang 050043, China

R. Tian · X. Zhang · S. Li
Department of Engineering Mechanics, Shijiazhuang
Tiedao University, Shijiazhuang 050043, China

1 Introduction

With the tremendous booming of technology development, the requirements for low-frequency vibration control strategies considerably increase. Therefore, quasi-zero stiffness vibration isolators (QZSVIs) with “high static stiffness, low dynamic stiffness” gain most concern, especially in the fields puzzled by the contradiction between a wide vibration isolation frequency band and a desired load bearing capacity [1–6]. At present, one of the key objectives of QZSVIs is to inhibit the stiffness hardening phenomenon, broaden the QZS interval, and improve the attenuation effect of ultra-low frequency vibration.

To improve the ultra-low-frequency vibration isolation performance of QZSVIs, current negative stiffness mechanisms mainly use pre-compressed smooth and discontinuous (SD) oscillators [7, 8], roller-cam mechanisms [9], magnetic rings [10, 11], X-shaped structures [12, 13], bionic structures [14] and buckling beams [15–17], etc. The pre-compressed SD oscillator has negative stiffness when the displacement is relatively small, and the negative stiffness value gradually vanishes with the increase in displacement [18]. To make the vibrator stable, the minimum point of the equivalent stiffness of SD oscillators is set to be approximately zero by paralleling positive stiffness element, constructing the conventional QZSVI [19]. Further, some scholars paralleled multiple sets of pre-compressed SD oscillators in different directions to obtain a multi-directional low-frequency vibration isolation capability [20]. To improve the applicability of QZSVIs, SD oscillators can be replaced by the cam-roller structure whose restoring force can be adjusted by modifying the cam curve [21, 22]. When the displacement range is relatively small (usually a few millimeters to tens of millimeters), the ring-magnet structure can provide a similar motion pattern and negative stiffness characteristics as the two structures mentioned above [23]. These structures can slightly expand their QZS region by constrains the changing rate of the stiffness when constructing QZSVIs, whose vibration isolation performance is still limited by stiffness hardening due to their complex negative stiffness characteristics and unmatched positive stiffness elements. Further, QZSVIs, constituted by coupling X-shaped structures or bionic structures with positive stiffness elements, commonly possess asymmetric restoring force,

resulting in the restraint on stiffness hardening [24, 25]. Hence, they have lower natural frequency and wider vibration isolation frequency band, which is one of the hot spots in the research of QZSVIs. Gatti et al. proposed a double-quasi-zero-stiffness vibration isolator mainly composed of four linear springs arranged in an X-shaped configuration. This isolator can obtain a relatively low dynamic stiffness under large displacement response due to a sigmoidal shape characteristic generated by the X-shaped spring configuration [26]. With the increasing maturity of 3D printing technology, many beams made up of PLA utilize the buckling phenomenon to provide negative stiffness with fewer shape limitations. By adjusting the size and shape of their structure, diverse negative stiffness characteristics can be achieved to meet the demands of QZSVIs. The dimensions of these beams can be much smaller than mechanical structures, which makes 3D printed buckling beams have great application potential in the fields of low-frequency vibration control and sound insulation [27–29].

Stiffness compensation methods are of considerable significance to improve the ultra-low frequency performance of QZSVIs [30, 31]. Linear stiffness compensation methods originating from ordinary QZSVI typically use various categories of compression, tension, or torsion springs to produce positive stiffness to implement QZS at equilibrium positions. This method is simple, but using linear springs can only alter the value of equivalent stiffness, and has no influence on the changing rate. Recently, nonlinear stiffness compensation methods have gradually attracted more attention. The nonlinear stiffness compensation method uses a variety of elements to provide positive stiffness varying with displacement, satisfying the demand of stiffness compensation while reducing stiffness hardening. Because like poles repel each other, the value and the changing rate of the equivalent stiffness can be changed at the same time due to the variable stiffness property of the magnet [1, 32]. The key problem of nonlinear stiffness compensation methods that need to be further studied is that the nonlinear characteristics of these nonlinear stiffness compensation elements are complicated, which is not convenient to flexibly design according to the requirements of stiffness compensation. The stiffness hardening phenomenon still exists and, typically, is uncontrollable. In addition, the development of QZSVIs has entered a bottleneck that only a

few vibration isolators have been experimentally proved to have a natural frequency less than 3 Hz, and the natural frequency cannot be stabilized in the range of 1 to 3 Hz. Some nonlinear elements have low availability and are easy to interfere with the system, such as magnets. The existence of magnets in the system is easy to cause eddy current effect or magnetization of other components, resulting in thermal load or magnetic interference [33]. When the distance between two magnetic poles is relatively large (about tens of millimeters), the magnetic force would rapidly decay to zero, losing the stiffness compensation effect. These problems heavily confine the size and application range of QZSVIs containing magnets. Based on 3D printing technology, beams made from materials, such as PLA, nylon, and ABS, can control deformation patterns through different configurations to provide nonlinear restoring force and variable stiffness characteristics required for stiffness compensation [29, 34, 35]. The beams providing positive stiffness and the buckling beams providing negative stiffness can be processed by additive manufacturing simultaneously to form integrated QZSVIs [16, 36–38]. However, integrated QZSVIs still lacks long-term and mature engineering application examples. After being subjected to alternating loads in vibration environment, their life expectancies and reliability remain to be studied.

The above studies indicate that the research on QZSVIs is still nested in proposing new positive and negative stiffness mechanisms, and combining them to obtain QZSVIs with weak stiffness hardening, low natural frequencies, and wide vibration isolation frequency bands. Although, some studies on QZSVIs have started exploring the matching degree of positive and negative stiffness. However, the problem of stiffness hardening remains unsolved. The reason might be that the mechanical properties of the stiffness compensation elements are complicated, which haunts the reverse design according to the demand of stiffness compensation. Hence, the matching degree of the positive and negative stiffness elements deteriorates with the increase in displacement, leading to an inevitable generation of stiffness hardening in the neighborhood of the equilibrium position of the isolator, which not only limits the low-frequency vibration isolation performance but also affects the system stability. This study attempts to inhibit stiffness hardening radically through a nonlinear mirrored

stiffness design method (NMSM) and reveal the applicable condition of the NMSM. The basis of the NMSM is a type of nonlinear spring (NS), which can easily achieve desirable nonlinear restoring force and variable stiffness characteristics by reasonably adjusting its pitch distribution. By designing the NS according to a specific negative stiffness curve, a positive stiffness curve, which possesses an approximate mirror-image relationship with the targeted negative stiffness curve, can be obtained in the QZS region. Due to the remarkable availability of the NS, the NMSM has a broad potential application prospect. As long as the negative stiffness mechanism meets the applicable conditions, this method can be used to design suitable NSs to suppress the stiffness hardening phenomenon in the QZS region and improve the performance of QZSVIs.

The contents are arranged as follows: In Sect. 2, the mechanism of stiffness hardening in QZSVI is revealed, and the origination of NMSM is expounded. In Sect. 3, the principle and detail process of NMSM are proposed, and the function of equivalent stiffness of NS is clarified. The QZS implementation results of NMSM, linear stiffness compensation method and nonlinear stiffness compensation method are compared. In Sect. 4, QZSVI is constructed with NMSM for different negative stiffness characteristics to verify the effectiveness of NMSM. The design method of NS is presented. The vibration transmission results of QZSVI obtained by NMSM, linear stiffness compensation method and nonlinear stiffness compensation method are compared. In Sect. 5, vibration experiments are used to verify the correctness of NMSM. The conclusions are in Sect. 6.

2 Nonlinear mirrored-stiffness design method

To reduce stiffness hardening, it is necessary to reveal the mechanism of implementing QZS. Figure 1 summarizes the mechanisms of achieving QZS through the linear stiffness compensation method, nonlinear stiffness compensation method, and the NMSM. The linear stiffness compensation method is shown in Fig. 1a. The nonlinear compensation method is demonstrated using magnets and X-structures, as shown in Fig. 1b. To illustrate the mechanism of the NMSM, the sketch diagrams of restoring force and stiffness exhibit the ideal results, as shown in Fig. 1c.

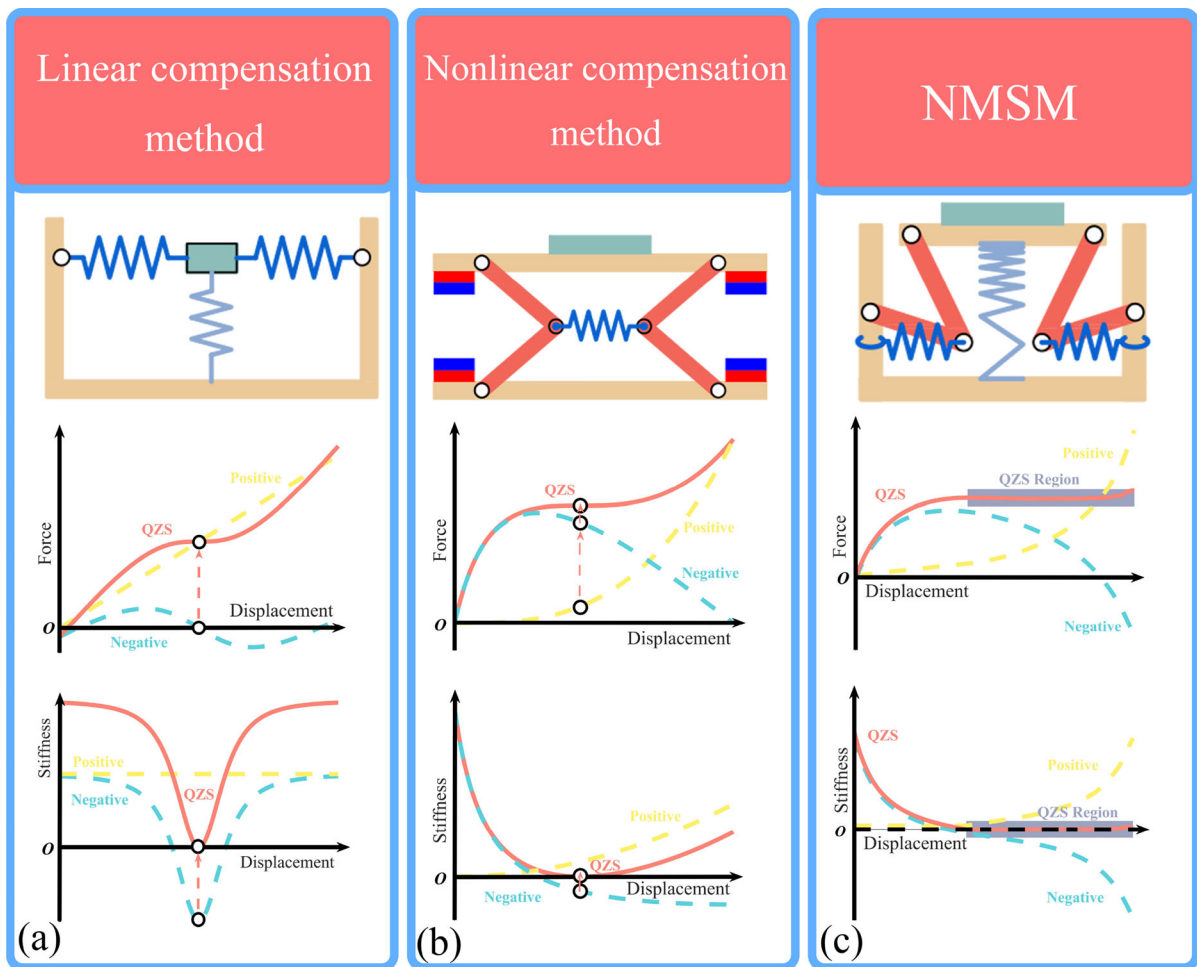


Fig. 1 The comparison diagram of different methods for implementing the QZS property, **a** the linear compensation method, **b** the nonlinear compensation method and **c** the NMSM

In the sketch map, ‘Positive’, ‘Negative’ and ‘QZS’ are only used to represent the stiffness characteristics corresponding to the curve.

In Fig. 1a, the linear spring only increases the value of the equivalent stiffness of conventional QZSVIs, but does not affect the changing rate of the equivalent stiffness. Hence, the linear compensation method can only ensure that the positive and negative stiffness at the equilibrium position is approximate zero [39, 40]. In the vicinity of the equilibrium position, the equivalent stiffness tends to a fixed value with the rapid increase of displacement, manifesting as stiffness hardening.

In Fig. 1b, the variable stiffness characteristic of the magnet can be used to simultaneously change the value and changing rate of the equivalent stiffness. In

this case, the equivalent stiffness can be expressed as a polynomial function with respect to the displacement [30]. Hence, the nonlinear stiffness compensation method can constrain both the value and the changing rate of the equivalent stiffness. At present, only the first three sets of the stiffness coefficients can be determined in the neighborhood of the equilibrium position. The restoring force of the system presents a “platform-shape” as shown in Fig. 1b. These higher-order nonlinear components significantly affect the results when the displacement is relatively large, because these higher-order nonlinear components cannot be confined by the nonlinear stiffness compensation method. To ensure the system stability, the increasing rate of the stiffness of the magnet is required to be larger than the decreasing rate of the

stiffness of the X-type structure, resulting in the stiffness hardening.

It can be concluded that compared with the linear compensation method, the nonlinear stiffness compensation method weakens the stiffness hardening phenomenon to some extent by constraining the value and the changing rate of the equivalent stiffness, simultaneously. However, this method gradually invalids with the increase in the displacement. The reason is that the method cannot accurately constrain the high-order nonlinear components of both positive and negative stiffness elements. When the displacement is relatively large, the proportion of the higher-order nonlinear components increases, and stiffness hardening is induced.

Based on the idea of the linear and nonlinear stiffness compensation method, NMSM further constrains the higher-order nonlinear components of the positive and negative stiffness elements through configuring the shapes of these two curves a mirror image in a certain region, as shown in Fig. 1c. The NMSM can design NSs according to specific negative stiffness characteristics. By reasonably configuring the pitch distribution of the NS, the nonlinear components of each order can be adjusted to improve the matching degree of the stiffness elements. Under ideal conditions, the NS has enough coils, resulting in that its stiffness can approximately change with the compression amount continuously. Actually, the number of the coil is limited, and the stiffness can only achieve a step change with the amount of compression. However, NMSM can still considerably suppress stiffness hardening, only remaining a bounded small fluctuation of stiffness which is close to zero. In the QZS region of Fig. 1c, the NMSM significantly weakens stiffness hardening. The width of the QZS region in the diagram is much wider than that obtained by both linear and nonlinear compensation methods.

3 The mechanism of the NMSM

The mechanism of the NMSM is explained in Fig. 2.

As shown in Fig. 2a, the steps of the NMSM can be summarized as designing the pitch distribution of the NS based on the specific negative stiffness data, adjusting the shut position of each coil, producing positive stiffness varying with the effective number of the coil, neutralizing the specific negative stiffness

achieving QZS. The principle of NMSM to construct QZS region is shown in Fig. 2b. In the QZS region, the positive and the negative stiffness present a mirror-image relationship that the absolute values of the two are almost equal and their changing rates are opposite. The applicable condition of the NMSM is shown in Fig. 2c. When the stiffness of any constructions is less than zero, the changing rate of the stiffness with respect to the displacement x should meets

$$\frac{dK}{dx} \leq 0. \tag{1}$$

The applicable condition includes three practical situations that the changing rate of the stiffness with respect to the displacement approximately equals zero, smaller than zero, and far less than zero, as marked in Fig. 2c by black dash arrows. Equation (1) is derived from the realization mechanism of the variable stiffness of the NS, shown in Fig. 2d. In Fig. 2d, the pitch of the NS increases with the number of the coil. The pitch at the left end is the smallest, and the one at the right end is the largest. In the process of compression and deformation, the restoring force of the NS can be divided into two regions, the linear region and the nonlinear region. The linear region corresponds to the interval $[0, \chi_1]$, endpoint χ_1 equals $N\kappa_1$, where N denotes the number of the coil, and κ_1 is the smallest pitch. The endpoint χ_1 is the entrance of the QZS region and the start point of the nonlinear region of the NS. In the linear region, the effective number of the coil \tilde{N} does not change with the amount of compression. Hence, the nonlinear springs is equivalent to a linear spring. After entering the nonlinear region, the equivalent stiffness K_s increases with the decrease of the effective number of the coil \tilde{N} . The function relationship between the effective number of the coil and the equivalent stiffness of the NS is

$$K_s = \frac{k_{ini}}{\tilde{N}} \tag{2}$$

where k_{ini} is the fundamental stiffness of the NS. When the compression amount equals the endpoint χ_1 , the first coil is shut, the effective number of the coil becomes $N - 1$, and the equivalent stiffness increases by $N/(N - 1)$ times, which corresponds to the position of the gray arrows in Fig. 2d. As the amount of compression continues to increase, the gray dashed line in the pitch diagram in Fig. 2d moves upward, corresponding to the dashed line in the stiffness

Fig. 2 The mechanism of the NMSM, **a** the procedure of the NMSM, **b** the sketch map of the equivalent stiffness, **c** the constraint condition for negative stiffness characteristics and **d** the variable stiffness mechanism of the nonlinear spring

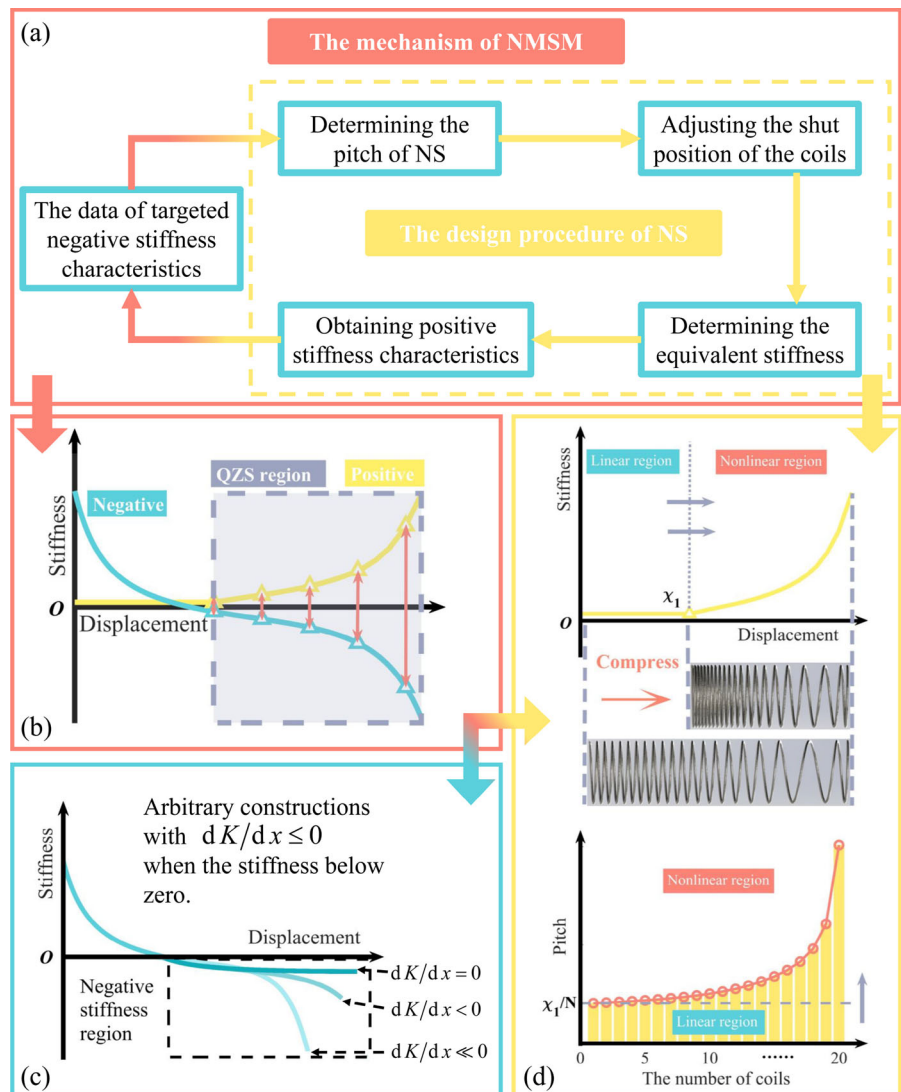


diagram moving to the right. In the pitch diagram, whenever the gray dashed line reaches the pitch value of the next coil (the dashed line reaches the top of the next yellow cylinder), suggesting that this coil is shut, the effective number of the coil is reduced, and the equivalent stiffness is increased. It should be noted that the position of χ_1 is specifically arranged in the negative stiffness region of the targeted negatives stiffness curve to ensure the effectiveness of the NMSM. If the position of χ_1 is located in the positive part of the targeted negatives stiffness curve, the stiffness hardening phenomenon is likely to be aggravated since the inherent-positive stiffness of the

targeted curve is enlarged by the nonlinear-positive stiffness introduced by the NS.

From the above analysis, it can be seen that in the compression process of the NS, the effective number of the coil can only monotonically decrease or be a fixed value with the increase in the compression amount, but cannot be increased. Hence, the NMSM can only design the NSs based on the negative stiffness structures satisfying the condition in Fig. 2c.

The relationship between the effective stiffness of the NS and the compression amount (represented by the displacement x) is

$$K_s(x, \rho) = \frac{k_{ini}}{\tilde{N}(x, \rho)} = \frac{k_{ini}}{N - \sum_{i=1}^N H(x - \rho_i)} \tag{3}$$

where $H(x - \rho_i)$ is Heaviside function. ρ_i is the compression amount corresponding to the points where the coil is shut. The formula used to calculation ρ_i is

$$\rho_i = \sum_{i=2}^N [(\kappa_i - \kappa_{i-1} - d)(N - (i - 1))], \tag{4}$$

where d is the wire diameter of the NS, $\rho_0 = 0$, and $\rho_1 = \chi_1$.

According to Eq. (3) and Eq. (4), by reasonably distributing the pitch κ_i , the effective number of the coils \tilde{N} can be changed at the specific compression amount ρ_i , which assures NSs can present different nonlinear stiffness characteristics. When the number of the coil N is sufficient, the effective stiffness shown in Eq. (3) can be changed continuously with the compression amount to achieve the mirror-image relationship shown in Fig. 1. When the stiffness curve of the NS meets the mirror-image relationship with the targeted negative stiffness, it indicates that the positive and the negative stiffness have been matched, and the stiffness hardening phenomenon in the QZS region is suppressed. Actually, the number of the coil is finite. Therefore, the stiffness of the NS practically exhibits a step change with the amount of compression. After coupled with the targeted negative stiffness structure, the equivalent stiffness inevitably shows a slight fluctuation close to zero in the QZS region, but it can still significantly weaken the stiffness hardening phenomenon, as shown in Fig. 3.

Figure 3a, b show that under the same rated load, 87 N, the number of the coil limits the performance of the NMSM, leading to a generation of a slight fluctuation of stiffness close to zero in the QZS region. However, compared with the results obtained by the linear and the nonlinear stiffness compensation method, stiffness hardening in the neighborhood of the equilibrium position caused by the NMSM is significantly weakened. It is clear that the equivalent stiffness obtained by the NMSM is the lowest and the QZS region is the widest. To obtain the optimal result for restraining stiffness hardening, the starting point of the QZS region should be located in the nonlinear region of the restoring force of the NS. Hence, according to Fig. 2, the starting point of the QZS region should be the

endpoint of the linear region, i.e., $x = \chi_1$. To probe the phenomenon of the slight fluctuation of the equivalent stiffness in the QZS region, the upper boundary envelope K_{sup} and the lower boundary envelope K_{sdo} of the fluctuations can be obtained according to Eq. (3) and Eq. (4). Hence,

$$K_{sup} = \left[\frac{k_{ini}}{N - \sum_{i=1}^N H(x - \rho_i)} + \sum_{j=0}^p \mu_j x^j \right] \Big|_{x=\rho_i}, \tag{5}$$

$$K_{sdo} = 0, \tag{6}$$

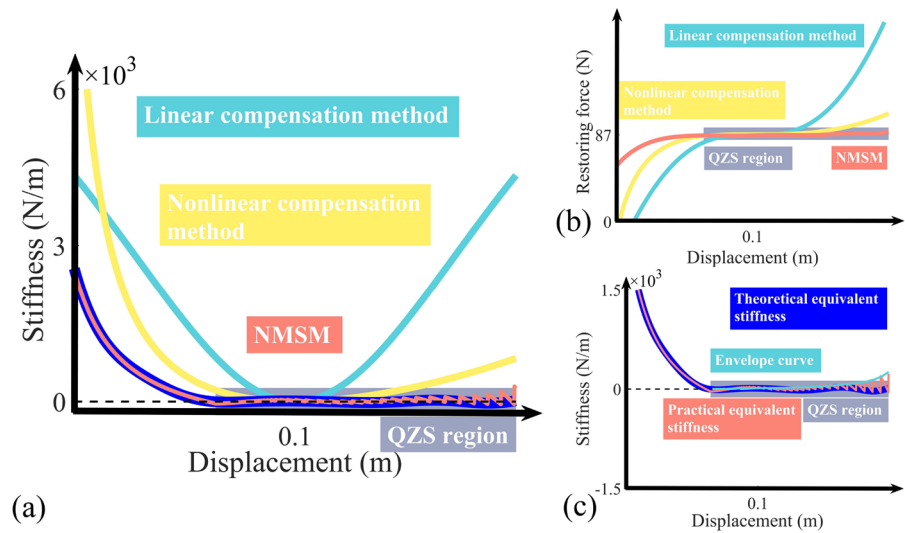
where p is the highest-order component of the nonlinear restoring force of the negative stiffness structure, μ_j is the nonlinear stiffness coefficient of the negative stiffness structure.

It can be seen from Fig. 3c that this small fluctuation only occurs in the QZS region, i.e., the nonlinear region of the NS. When the displacement is less than the starting point of the QZS region χ_1 , the sum of the Heaviside function in Eq. (5) stays zero. Hence, the effective number of the coil and the equivalent stiffness of the NS are not affected by the variation of the displacement. After entering the QZS region, the sum of the Heaviside function presents a step change with the increase in the displacement, resulting in the generation of the small fluctuation phenomenon and a continuous increase in the value of the upper boundary envelope. If the number of the coil approaches infinity, the sum of the Heaviside function would change continuously with the displacement. The equivalent stiffness of the NS equals the absolute value of the targeted negative stiffness at every shut position $x = \rho_i$, which can make the upper boundary envelope approach zero from the theoretical point of view, inhibit the small fluctuation phenomenon, and further weaken the stiffness hardening.

4 The validation of the NMSM

To validate the NMSM, a concave metastructure with different stiffness characteristics is proposed. The different negative stiffness due to the selection of the system parameters of the concave metastructure exactly corresponds to the three situations of Eq. (1). Hence, the CQZSVI can be obtained by combining the NSs designed by the NMSM and the concave metastructure. The effectiveness of the NMSM can be

Fig. 3 The equivalent stiffness diagram, **a** the comparison results of different methods, **b** the restoring force, **c** the partial enlarged diagram of the equivalent stiffness obtained by NMSM



verified by probing the statics property and the ultra-low-frequency vibration isolation performance of the CQZSVI.

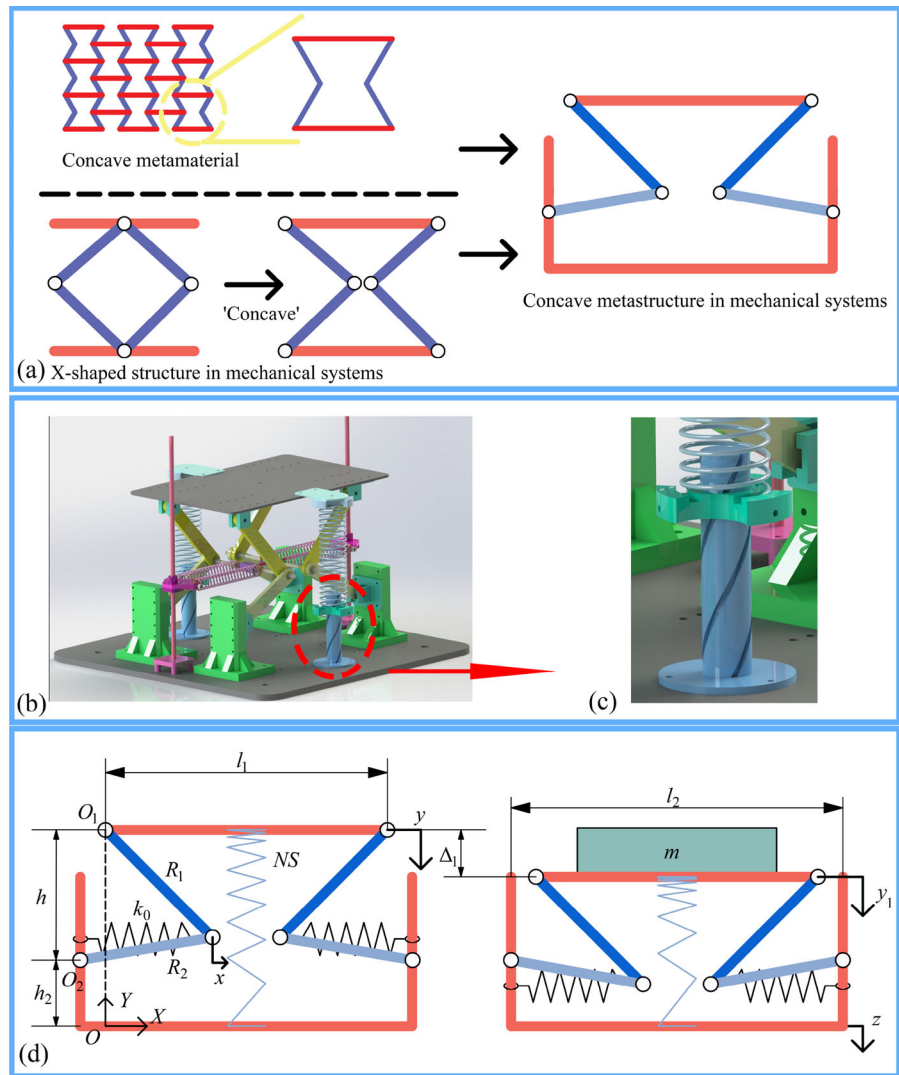
4.1 The structure of the CQZSVI

The structure and parameter setting of the CQZSVI are shown in Fig. 4. This vibration isolator is composed of the NSs designed by the NMSM and a concave metastructure. The concave metastructure is inspired by concave metamaterials with negative Poisson's ratio and X-shaped structures, attempting to obtain a variable stiffness property that its stiffness can vary from positive to negative with the increase in displacement [13, 41, 42], as shown in Fig. 4a. Furthermore, the displacement range of the concave metastructure is expanded by upraising the fixed position of the rods from the basement to obtain a desired variable stiffness property.

The yellow part in Fig. 4b is the main body of the concave metastructure. The arrangement of the yellow rods is obtained by imitating the configuration of X-shaped structure and the concave metamaterial. To minimize the influence of sliding friction caused by the joints of the rods, deep groove ball bearings are embedded in these joints. These bearings successfully suppress sliding friction. Hence, the concave metastructure mainly exhibits viscous damping characteristics, which is verified by the experiment of damping ratio in Sect. 5. The green parts are used to connect the concave metastructure with the lower plate and to

broaden the displacement range of the upper plate. Due to the green parts, the upper plate can move downward farther that the joints between two inter-linked rods is lower than the connected point between the green parts and the yellow parts, which makes the concave metastructure obtain various negative stiffness properties. The outer end of the linear spring in the purple part is connected to a flange bearing, and the inner end is connected to the hinge joint of the concave metastructure. When the upper plate moves downward, the displacement of the upper plate is transferred to the linear spring through the hinge joint, changing the compression amount of the linear springs. Through the structural design (the purple parts), it is ensured that the linear spring has the same height with the hinge joint and parallels to the upper and lower plates. Based on the different system parameters, the concave metastructure can provide positive or negative stiffness characteristics to meet the requirements of verifying the NMSM. The blue springs in Fig. 4 is the NS designed by the NMSM (the variation of pitch is not reflected, which has no effects on the exhibition of the structure). The nonlinear spring connects with the concave metastructure through two blue pedestals, as shown in Fig. 4b, c. The pedestals have grooves which trap the nonlinear spring and prevent it from sliding sideways during compression, as shown in Fig. 4c. The height of the lower pedestal is fixed after being adjusted, while the upper pedestal is connected with the upper plate. Hence, the nonlinear spring is compressed when the upper plate moves downward.

Fig. 4 The sketch maps of the CQZSVI and the system parameters, **a** the inspiration of the CQZSVI, **b**, **c** the three-dimension diagrams of the CQZSVI, **d** the diagram of the system parameters



At the equilibrium position as shown in Fig. 4d, the NS provides positive stiffness, and the concave metastructure provides negative stiffness. By combining the NS and the concave metastructure, the QZS property can be achieved.

Figure 4d shows the parameter settings of the CQZSVI at no-load and rated load. R_1 and R_2 are the length of the upper and lower rod, respectively. l_1 and l_2 are the length of the upper plate and the base, respectively. h is the initial height, h_2 is the lift height, the stiffness of the linear spring is k_0 , z is the excitation of displacement. y is the displacement of the upper plate from the initial position where all the springs are at the original length. The horizontal displacement of the hinge joint of the rods is x . When the CQZSVI

bears the rated load and the upper plate is in the equilibrium position, the displacement of the upper plate is y_1 . The discrepancy between y and y_1 is Δ_1 .

4.2 The statics analysis of the concave metastructure

To study the inherent stiffness characteristics of the concave metastructure as shown in Fig. 4, The NSs are temporarily ignored and only the influence of the linear spring on the restoring force is considered. Firstly, the functional relationship between the displacement of the upper plate y and the displacement of the hinge joint x is established. The origin and the coordinate system OXY are shown in Fig. 4d. When

the upper plate moves, the coordinates of the hinge joints can be represented by the intersection point of two circles with a radius of R_1 and R_2 , and a center of the O_1 and O_2 , respectively.

$$\begin{cases} x_0^2 + (y_0 - (h + h_2 - y))^2 = R_1^2 \\ (x_0 - \Delta_0)^2 + (y_0 - h_2)^2 = R_2^2 \end{cases}, \tag{7}$$

where $\Delta_0 = (l_1 - l_2)/2$.

The initial coordinate of the hinge joint (x_0, y_0) and the coordinate after the upper plate shifts (x_1, y_1) can be obtained by Eq. (7).

$$\begin{cases} x_0 = \frac{1}{2(h^2 + \Delta_0^2)} ((h^2 + R_1^2 - R_2^2)\Delta_0 + \Delta_0^3 - \sigma_1\sigma_2hM_0) \\ y_0 = \frac{1}{2(h^2 + \Delta_0^2)} (h(h^2 + 2hh_2 - R_1^2 + R_2^2) + (h + 2h_2)\Delta_0^2 - \sigma_1\sigma_2M_0) \end{cases}, \tag{8}$$

$$\begin{cases} x_1 = \frac{1}{2((h - y)^2 + \Delta_0^2)} ((R_1^2 - R_2^2 + (h - y)^2)\Delta_0 + \Delta_0^3 - \sigma_1\sigma_2hM_1 + \sigma_1\sigma_2yM_1) \\ y_1 = \frac{1}{2((h - y)^2 + \Delta_0^2)} ((R_2^2 - R_1^2 + (h - y)(h + 2h_2 - y))(h - y) + (h + 2h_2 - y)\Delta_0^2 - \sigma_1\sigma_2M_2) \end{cases}, \tag{9}$$

where $M_0 = \sqrt{-(h^2 - (R_1 - R_2)^2 + \Delta_0^2)(h^2 - (R_1 + R_2)^2 + \Delta_0^2)}$,
 $M_1 = \sqrt{-((h - y)^2 - (R_1 - R_2)^2 + \Delta_0^2)((h - y)^2 - (R_1 + R_2)^2 + \Delta_0^2)}$,
 $M_2 = \sqrt{-\Delta_0^2((h - y)^2 - (R_1 - R_2)^2 + \Delta_0^2)((h - y)^2 - (R_1 + R_2)^2 + \Delta_0^2)}$.

To simplify the above equations, set

$$\sigma_1 = \begin{cases} 1 & x_1 = \max(x_1) \\ -1 & x_1 \neq \max(x_1) \end{cases}, \tag{10}$$

$$\sigma_2 = \begin{cases} 1 & \Delta_0 > 0 \\ -1 & \Delta_0 \leq 0 \end{cases}. \tag{11}$$

By combining Eqs. (8)-(11), the displacement of the hinge joint $x(y)$ can be obtained as

$$\begin{aligned} x(y) = x_1 - x_0 = & \frac{1}{2((h - y)^2 + \Delta_0^2)} \\ & ((R_1^2 - R_2^2 + (h - y)^2)\Delta_0 + \Delta_0^3 - \sigma_1\sigma_2hM_1 + \sigma_1\sigma_2yM_1) \\ & - \frac{1}{2(h^2 + \Delta_0^2)} ((h^2 + R_1^2 - R_2^2)\Delta_0 + \Delta_0^3 - \sigma_1\sigma_2hM_0). \end{aligned} \tag{12}$$

To study the statics property of the concave metastructure, it is necessary to solve the range of displacement in Eq. (12) to distinguish different types of the restoring force and the stiffness characteristics.

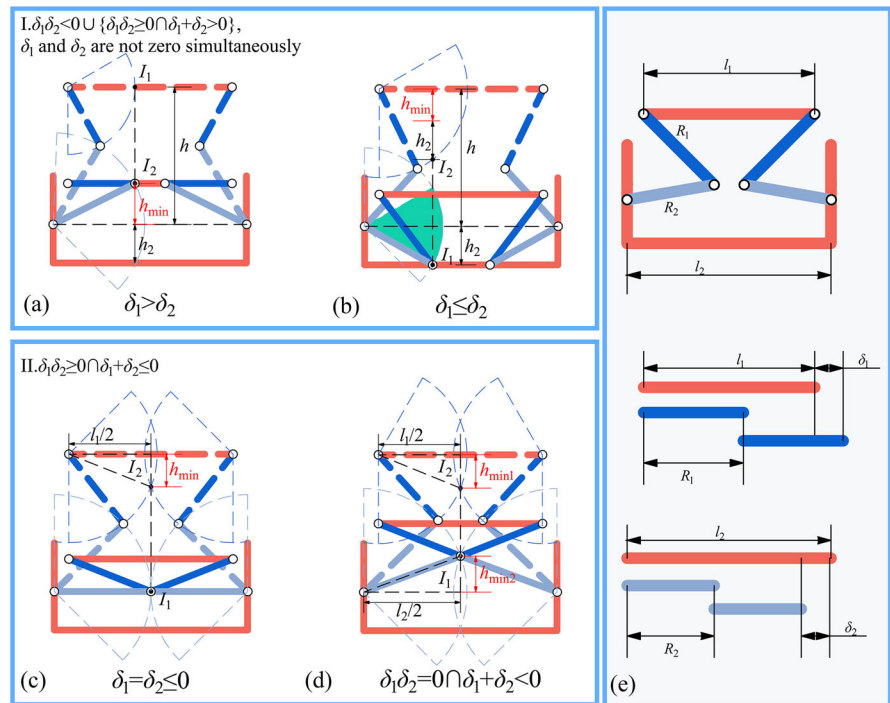
Two overlap parameters are set as

$$\begin{cases} \delta_1 = l_1 - 2R_1 \\ \delta_2 = l_2 - 2R_2 \end{cases}. \tag{13}$$

Based on the different overlap parameters, this concave metastructure can be classified into two displacement modes (I and II) with different limitation situations of the displacement, as shown in Fig. 5.

In Fig. 5, the dashed lines represent the ideal motion trajectories of the upper and the lower rods. The diagram of each configuration shows the case that the upper plate moves downward and reaches the limit position. The white circle is the joint between two interlinked rods. As shown in Fig. 5e, the overlap parameter δ_1 represents the relative length relation between the length of the upper plate and the length of the upper rod, while δ_2 represents the relative length relation between the length of the base and the length

Fig. 5 The geometric relationship of the concave metastructure, **a, b** the different configurations of Type I, **c, d** the different configurations of Type II, **e** the sketch diagram of the overlap parameters



of the lower rod. In type I, these two joints will not collide with each other within the entire displacement range of the upper plate. But, in type II, these two hinge joints intersect at the limit position of the upper plate when both of the overlap parameters are less than or equal to zero, restricting the displacement range of the upper plate.

Then, the maximum y_{\max} and the minimum y_{\min} of the displacement y are

$$\begin{cases} y_{\min} = h - h_{\max} \\ y_{\max} = h - h_{\min} \end{cases} \quad (14)$$

where h_{\min} and h_{\max} correspond the minimum and maximum of the initial height h , respectively.

Further, the maximum and the minimum of the initial height for each case are derived. As can be seen from Fig. 5a, when $\delta_1 > \delta_2$, the point I_1 moves downward with the upper plate to reach the limit position I_2 . Hence, the minimum of the initial height is

$$h_{\min} = y_{I_2} - h_2 = \sqrt{R_2^2 - R_1^2 + 2R_1\Delta_0} - \Delta_0^2, \quad (15)$$

where y_{I_2} is the vertical coordinate of the point I_2 .

Similarly, when $\delta_1 \leq \delta_2$ as shown in Fig. 5b, the minimum value is

$$h_{\min} = h - y_{I_2} = \sqrt{R_1^2 - \frac{R_2^2}{2} - \Delta_0^2 + \frac{1}{2}R_2^2 \cos(2\theta_2) - 2R_2\Delta_0 \sin(\theta_2)} - h_2, \quad (16)$$

As shown in Fig. 5c, d, the limit of the upper plate occurs at the position where the hinge joints contact each other. According to the geometric relationship and the symmetry of the metastructure, the minimum value can be obtained.

$$h_{\min} = h_{\min 1} + h_{\min 2} = \sqrt{R_1^2 - \left(\frac{l_1}{2}\right)^2} + \sqrt{R_2^2 - \left(\frac{l_2}{2}\right)^2} \quad (17)$$

The maximum of the initial height of the above situations is

$$h_{\max} = \sqrt{(R_1 + R_2)^2 - \Delta_0^2}. \quad (18)$$

Then, the displacement range of the upper plate can be obtained by combining Eq. (15) with Eq. (18) and substituting them into Eq. (14). Under the constraint of Eq. (14), it is assumed that the upper plate of the metastructure without the load shown in Fig. 4 is subject to an external force F_1 . According to the law of

conservation of energy, one equation can be obtained as

$$\int_0^y F_1 dy = 2 \times \frac{1}{2} k_0 x^2(y), \tag{19}$$

The restoring force F_1 and equivalent stiffness K_1 of the superstructure can be obtained by combining Eqs. (14) and (19).

$$\begin{cases} F_1 = 2k_0x(y) \frac{dx(y)}{dy} = 2k_0f_1(y) \\ K_1 = 2k_0 \frac{df_1(y)}{dy} \end{cases}, \tag{20}$$

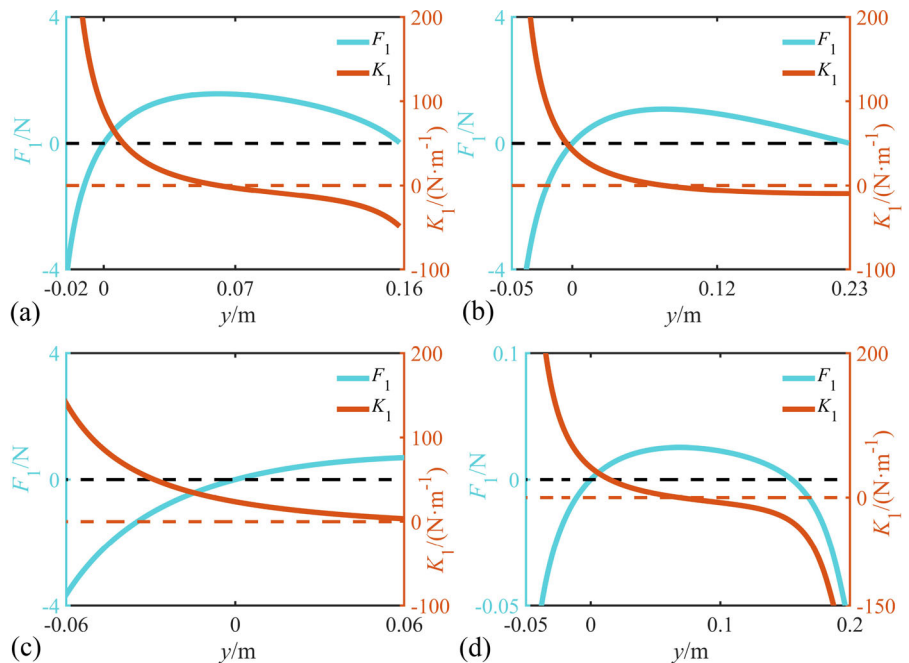
where $\frac{dx(y)}{dy} = (2(h-y)((R_1^2 - R_2^2 + (h-y)^2)\Delta_0 + \Delta_0^3 - \sigma_1\sigma_2hM_1 + \sigma_1\sigma_2yM_1) + ((h-y)^2 + \Delta_0^2)(-2(h-y)\Delta_0 + \sigma_1\sigma_2M_1 - (2h(h-y)(h^2 - R_1^2 - R_2^2 - 2hy + y^2 + \Delta_0^2)\sigma_1\sigma_2) / M_1 + (2(h-y)y(h^2 - R_1^2 - R_2^2 - 2hy + y^2 + \Delta_0^2)\sigma_1\sigma_2) / \Delta_0^2\sigma_1\sigma_2M_1.M_1)) / (2((h-y)^2 + \Delta_0^2)^2)$.

According to different overlap parameters, Eq. (20) can exhibit different stiffness characteristics of the concave superstructure, as shown in Fig. 6. The parameters used to plot Fig. 6 are shown in Table 2, which are selected primarily based on the four

different segments divided by the overlap parameters and on the actual size of the vibration test bench to completely demonstrate the mechanical properties of the concave metastructure and to prepare for the fabrication of the prototype. The cyan solid line in the figure represents the restoring force, and the red solid line is the equivalent stiffness. The black and the red dashed lines are the zero scale lines of the restoring force and the stiffness, respectively.

Figure 6 indicates that the concave metastructure exhibits either positive or negative stiffness characteristics with different overlap parameters. When the displacement is relatively small, these configurations all present a positive stiffness characteristic which decreases monotonically, and the restoring force increases with the displacement. When the restoring force reaches a peak, the equivalent stiffness is zero, as shown in Fig. 6a, b, d. Then, as the displacement continues to increase, these configurations enter the negative stiffness interval, and the restoring force gradually decreases. There are some discrepancies between the negative stiffness characteristics. When $\delta_1 = \delta_2 \neq 0$, as shown in Fig. 6b, the negative stiffness tends to a constant with the increase in the displacement. When $\delta_1 \neq \delta_2$, the negative stiffness decreases with the increase in the displacement as

Fig. 6 The sketch diagram of the restoring force and the equivalent stiffness characteristics of the concave metastructure, **a** $\delta_1 > \delta_2$, **b** $\delta_1 = \delta_2 \neq 0$, **c** $\delta_1 = \delta_2 = 0$, **d** $\delta_1 < \delta_2$



shown in Fig. 6a, d. It is worth noting that the negative stiffness decreases more sharply in Fig. 6d, i.e. the slope of the curve is much smaller than that in Fig. 6a. This phenomenon indicates that the negative stiffness of the system in Fig. 6d is more sensitive to the variation of the displacement, and the nonlinear characteristics are stronger. The reason for this sharply decreases is that, when the hinge joint crosses the horizontal black dashed line in Fig. 5d from the top to the bottom, the direction of its movement will flip instantaneously (for example, the left hinge joint, which originally moves to the right, will immediately move to the left after crossing the line). The crossing conditions can be expressed as

$$\arcsin\left(\frac{1}{2R_2(h^2 + \Delta_0^2)}((h^2 + R_1^2 - R_2^2)\Delta_0 + \Delta_0^3 - \sigma_1\sigma_2hM_0) - \frac{\Delta_0}{R_2}\right) < \arccos\left(\frac{h_2}{R_2}\right). \tag{21}$$

Equation (21) denotes that the initial position of the hinge joint is higher than the green area in Fig. 5. Moreover, Eq. (21) ensures that the linear spring keeps in the stretched state avoiding the second overturning of the direction of the force. When $\delta_1 = \delta_2 = 0$ as shown in Fig. 6c, the metastructure only has positive stiffness, which monotonically decreases with the displacement and tends to zero at the limit position of the upper plate. This stiffness characteristic is similar to many existing X-shaped structures and bionic structures.

These three different negative stiffness characteristics correspond to the three typical cases contained in Eq. (1). By using the NMSM to design NSs and construct CQZSVIs based on the above situations, the effectiveness of the NMSM can be verified through studying the restoring force and the equivalent stiffness of the CQZSVI.

4.3 The NS designed by the NMSM

With the development of the research about QZSVIs, stiffness compensation methods have been ameliorated from linear to nonlinear, but shortcomings still exist. For instance, the magnetic field interference brought by the application of magnets typically causes eddy current effect and generates unexpected restoring force [33]. 3D printed components such as beams and plates are subjected to alternating loads in a

vibrational environment, resulting in a relatively short life expectancy.

To overcome the above difficulties, NSs, which do not have harsh dimensional requirements and have a flexible and adjustable compression range, can be constructed using the NMSM. By reasonably designing the pitch of each coil, the equivalent stiffness of the NS can be changed as the effective number of the coil changes at a specific compression amount $x = \rho_i$. Moreover, based on the NMSM, the data of the negative stiffness properties can be used to manufacture the NSs as long as the applicable condition in Eq. (1) is satisfied. Hence, the NMSM overcomes the drawback that the highest order of the nonlinearity of the NS is restrained as three. The upper limits of the performance of the NS significantly soars. Therefore, using the NS as a nonlinear stiffness compensation element has a broad application prospect. The sketch map of the NS structure is shown in Fig. 7.

As the design process is the same, the NMSM is used to design an NS only by taking the negative stiffness curve shown in Fig. 6a as an example. In other cases, the results of coupled restoring force and equivalent stiffness are directly displayed. First, the number of the coil N and the wire diameter d of the NS are determined. The absolute values of the negative stiffness shown in Fig. 6a are expressed as a polynomial function

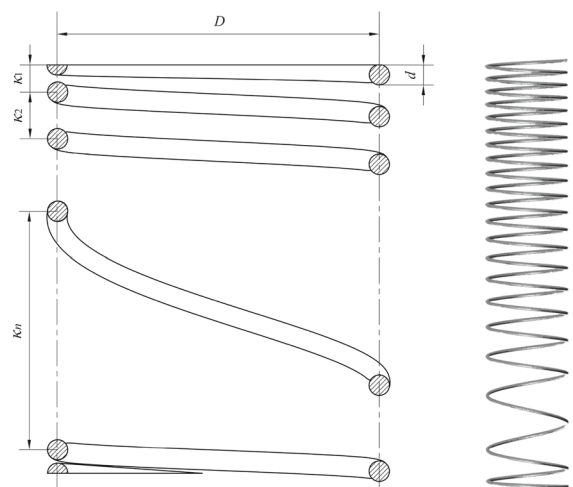


Fig. 7 The sketch diagram of NS obtained by NMSM

$$K_1 = \sum_{j=0}^p \tilde{\mu}_j x^j, \tag{22}$$

where $\tilde{\mu}_j$ is the coefficients. Substituting the maximum displacement y_{\max} in Eq. (14) into Eq. (22), the absolute stiffness of the negative stiffness mechanism at the displacement limitation K_{1end} is obtained, and then the stiffness $k_{0i} (i = 1, 2, 3, \dots, N)$ and compression value $\rho_{0i} (i = 1, 2, 3, \dots, N)$ corresponding to each shut position are calculated.

$$k_{0i} = \frac{K_{1end}}{N - (i - 1)} \tag{23}$$

$$k_{0i} - \sum_{j=0}^p \tilde{\mu}_j \rho_{0j}^i = 0s \tag{24}$$

Combining Eq. (23) and Eq. (24) and considering the influence of the wire diameter on the compression value, the pitch κ_{0i} of each coil and the middle diameter D can be obtained.

$$\kappa_{0i} = \begin{cases} \frac{\rho_{0i}}{N} + d, & i = 1 \\ \frac{\rho_{0i} - \rho_{0(i-1)}}{N - (i - 1)} + \kappa_{0(i-1)} + d, & i > 1 \end{cases} \tag{25}$$

$$D = \left(\frac{Gd^4}{0.8K_{1end}} \right)^{(1/3)} \tag{26}$$

During manufacturing, NS is restricted by the spring machine and the wire material, whose maximum pitch κ_{\max} needs to satisfy the requirement $\kappa_{\max} \leq 1.2D$. When low-order nonlinear components constitute the majority of the restoring force of the NS, the results obtained by Eq. (25) typically do not meet the above requirement. Hence, the pitch κ_{0i} needs to be modified. Set the maximum pitch after correction to be $\kappa_{1\max}$, and the maximum pitch before correction to be $\kappa_{0\max}$. After the modification, the pitch of the NS satisfies the following function

$$\kappa_{1i} = \kappa_{0i} + \frac{\Gamma_i(\kappa_{1\max} - \kappa_{0\max})}{\sum_{i=1}^{N-1} \Gamma_i}, \tag{27}$$

where $\Gamma_i = \{\Gamma_1, \Gamma_2, \Gamma_3, \dots, \Gamma_{N-1}\} = \{\Gamma_1, \Gamma_1^q, \Gamma_2^{2q}, \dots, \Gamma_{N-1}^{(N-2)q}\}$, $\Gamma_1 = [1.01, 1.08]$, and $q = [1, 1.2]$.

Based on Eq. (27), the modified restoring force F_{NSi} and the corresponding shut position ρ_{1i} of each coil can be obtained.

$$F_{NSi} = \begin{cases} \frac{K_{1end}\rho_{1i}}{N - (i - 1)}, & i = 1 \\ \frac{K_{1end}(\rho_{1i} - \rho_{1(i-1)})}{N - (i - 1)} + F_{NS(i-1)}, & i > 1 \end{cases} \tag{28}$$

$$\rho_{1i} = \begin{cases} (\kappa_{1i} - d)N, & i = 1 \\ ((\kappa_{1i} - d) - \kappa_{1(i-1)})(N - (i - 1)) + \rho_{1(i-1)}, & i > 1 \end{cases} \tag{29}$$

The combination of Eqs. (26), (27) and (29) can produce the NS required for coupling with the concave metastructure. In addition, Eq. (3) and Eq. (4) can be obtained by combining Eqs. (23), (27), (29) and Heaviside function.

By combining Eqs. (20), (23) and (28), the restoring force and the equivalent stiffness of the CQZSVIs are shown in Fig. 8, and the parameters are shown in Table 2 in ‘‘Appendix A’’.

Figure 8 exhibits that stiffness hardening can be significantly weakened when the NMSM is used to construct CQZSVIs by designing NSs based on the above negative stiffness characteristics and coupling with the concave metastructure. There are some discrepancies in Fig. 8. In terms of the load bearing performance, when $\delta_1 < \delta_2$, the CQZSVI has the maximum rated load, followed by the case $\delta_1 = \delta_2 \neq 0$, and the minimum payload corresponds to the case of $\delta_1 > \delta_2$. The payload shown in Fig. 8b is about 2 to 3 times larger than those in Fig. 8a, c. In terms of the length of the QZS region, when $\delta_1 = \delta_2 \neq 0$, the QZS region is the widest, accounting for about 62.65% of the total displacement range. The second is the case of $\delta_1 < \delta_2$, about 59.74%, and the region is the narrowest about 39.9% in the case of $\delta_1 > \delta_2$. Within these QZS regions, the average and the maximum stiffness values are less than 10 N/m, indicating that stiffness hardening is significantly inhibited compared to existing QZSVIs. Analyzing the pitch distributions of the NS, when $\delta_1 < \delta_2$, the pitch obviously increases with the number of the coil and the incremental amount is relatively uniform. When $\delta_1 > \delta_2$ as shown in Fig. 8a, the pitch increased significantly between the laps from 20 to 30th. When $\delta_1 = \delta_2 \neq 0$ as shown in Fig. 8c, the pitch increased

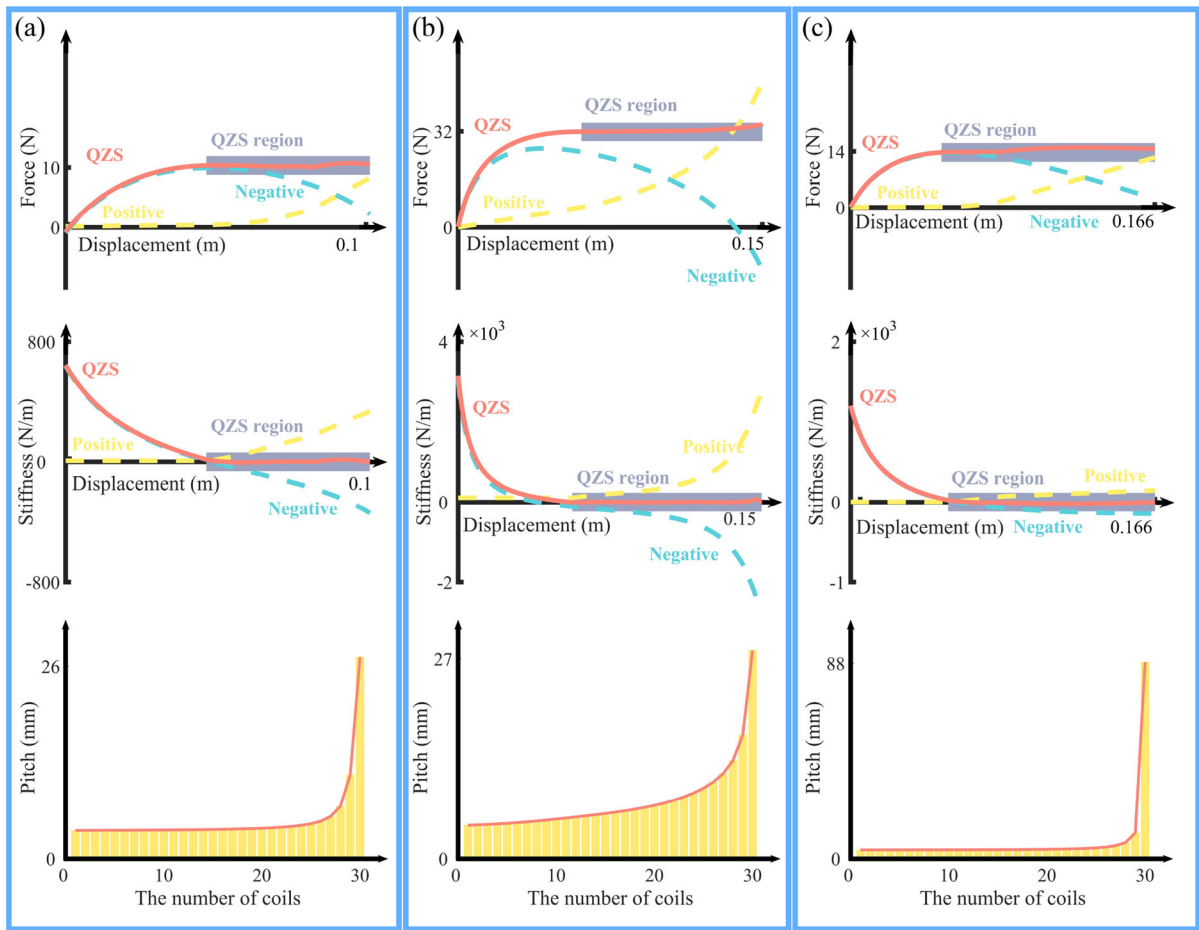


Fig. 8 Different situations for validating the correctness of the NMSM, **a** $\delta_1 > \delta_2$, **b** $\delta_1 < \delta_2$ and **c** $\delta_1 = \delta_2 \neq 0$

significantly only between the laps from 28 to 30th. When the increment of the pitch is too concentrated, as shown in Fig. 8a, c, it is easy to produce large manufacturing errors.

The above results prove that the stiffness hardening phenomenon can be significantly inhibited by using the NMSM to design the NS which meets the stiffness compensation requirements for the negative stiffness curve satisfying Eq. (1). By comprehensively considering the bearing capacity, the proportion of QZS regions and the fabricating precision of the NSs, the CQZSVI with the parameters satisfying $\delta_1 < \delta_2$ has the best synthetical statics performance.

4.4 The ultra-low-frequency vibration isolation performance of the CQZSVI

Further, the ultra-low-frequency vibration isolation performance of the CQZSVI constructed by the NMSM is analyzed. The dynamic differential equation of the CQZSVI is

$$m(\ddot{y}_1 + \ddot{z}) + c\dot{y}_1 + 2k_{qf1}(y) + F_{NSi} = mg, \tag{30}$$

where $y_1 = y - \Delta_1$, $z = p \cos(\omega t)$ is the displacement excitation, p is the excitation amplitude, ω is the excitation frequency. Generally, sliding friction is presented due to the rotation of the joint, which has significant influence on the vibration response [42–44]. To minimize the influence of the sliding friction on the performance of the CQZSVI, deep groove ball bearings are embedded in the joints.

Hence, viscous damping is dominated and is considered in Eq. (30). c denotes the damping coefficient. The damping ratio is tested and verified in Sect. 5. g is the acceleration of gravity.

To simplify the calculation, a polynomial is used to represent the restoring force in Eq. (30)

$$2k_{QF1}(y) + F_{NSi} = \sum_{i=0}^9 a_{i+1}y_1^i, \tag{31}$$

where $a_{i+1}(i = 0, 1, 2, \dots, 9)$ is the coefficient of the polynomial and can be obtained by the least-square method. The fitting results are shown in Fig. 9, and the system parameters are shown in Table 2.

There are three configurations of the concave metastructure used to implement CQZSVIs with NSs. As shown in Fig. 9, the fitting results of Eq. (31) are accurate enough for reflecting the QZS region in each configuration obtained by combining the concave metastructure with the NS.

Hence, substituting Eq. (31) into Eq. (30), and introducing the following dimensionless transformations

$$L_1 = l_1, \quad t_1 = \frac{m}{c}, \quad Y_1 = \frac{y_1}{L_1}, \quad \tau = \frac{t}{t_1}, \quad C = \frac{ct_1}{m}, \quad A_{i+1} = \frac{t_1^2 L_1^{-i} a_{i+1}}{m}, \quad \varsigma = \frac{gt_1^2}{L_1}, \quad P = \frac{p\Omega^2}{L_1}, \quad \Omega = \omega t_1.$$

Equation (30) can be rewritten in a dimensionless form as

$$\ddot{Y}_1 + C\dot{Y}_1 + \sum_{i=0}^9 A_{i+1}Y_1^i = \varsigma + P \cos(\Omega\tau). \tag{32}$$

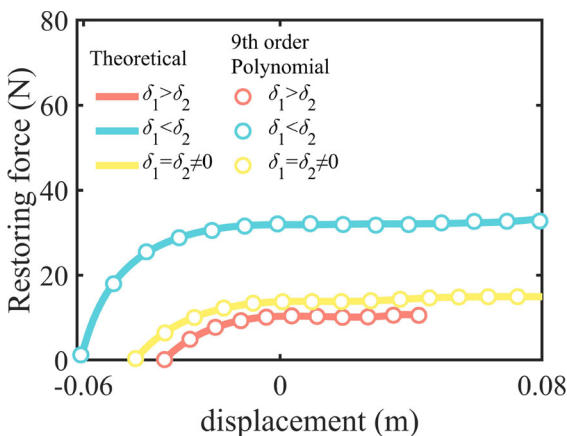


Fig. 9 The fitting results of the 9th-order polynomial in Eq. (31)

As the restoring force shown in Fig. 8 is asymmetric, the first-order approximate solution of Eq. (32) consists of two parts, one constant component and one harmonic component [30], which can be written as

$$Y_1 = p_0 + p_1 \cos(\Omega\tau + \theta), \tag{33}$$

where p_0 is the average value of the vibration response, p_1 is the amplitude of the harmonic component, θ denotes the phase.

Substituting Eq. (33) into Eq. (32), one can be obtained by the harmonic balance method.

$$\begin{aligned} \cos(\theta) = & \frac{p_1}{p\Omega^2} \left(A_9 + 2A_8p_0 + 3A_7p_0^2 + 4A_6p_0^3 \right. \\ & + 5A_5p_0^4 + 6A_4p_0^5 + 7A_3p_0^6 + 8A_2p_0^7 + 9A_1p_0^8 + \frac{3A_7p_1^2}{4} \\ & + 3A_6p_0p_1^2 + \frac{15}{2}A_5p_0^2p_1^2 + 15A_4p_0^3p_1^2 \\ & + \frac{105}{4}A_3p_0^4p_1^2 + 43A_2p_0^5p_1^2 + 63A_1p_0^6p_1^2 + \frac{5}{8}A_5p_1^4 \\ & + \frac{15}{4}A_4p_0p_1^4 + \frac{105}{8}A_3p_0^2p_1^4 + 35A_2p_0^3p_1^4 \\ & + \frac{315}{4}A_1p_0^4p_1^4 + \frac{35}{64}A_3p_1^6 + \frac{35}{8}A_2p_0p_1^6 \\ & \left. + \frac{315}{6}A_1p_0^2p_1^6 + \frac{63}{128}A_1p_1^8 - p_1\Omega \right) \end{aligned} \tag{34}$$

$$\sin(\theta) = \frac{-Cp_1}{P\Omega} \tag{35}$$

$$\begin{aligned} A_{10} - \varsigma + A_9p_0 + A_8p_0^2 + A_7p_0^3 + A_6p_0^4 + A_5p_0^5 + A_4p_0^6 \\ + A_3p_0^7 + A_2p_0^8 + \frac{A_8p_1^2}{2} + \frac{3}{2}A_7p_0p_1^2 + 3A_6p_0^2p_1^2 \\ + 5A_5p_0^3p_1^2 + \frac{15}{2}A_4p_0^4p_1^2 + \frac{21}{2}A_3p_0^5p_1^2 + 14A_2p_0^6p_1^2 \\ + 18A_1p_0^7p_1^2 + \frac{3}{8}A_6p_1^4 + \frac{15}{8}A_5p_0p_1^4 + \frac{45}{8}A_4p_0^2p_1^4 \\ + \frac{105}{8}A_3p_0^3p_1^4 + \frac{105}{4}A_2p_0^4p_1^4 + \frac{189}{4}A_1p_0^5p_1^4 \\ + \frac{5}{16}A_4p_1^6 + \frac{35}{16}A_3p_0p_1^6 + \frac{35}{4}A_2p_0^2p_1^6 \\ + \frac{105}{4}A_1p_0^3p_1^6 + \frac{35}{128}A_2p_1^8 + \frac{315}{128}A_1p_0p_1^8 = 0 \end{aligned} \tag{36}$$

The amplitude-frequency response function and vibration transmissibility T_d of the system can be obtained by combining Eqs. (34), (35) with Eq. (36).

$$\begin{aligned}
 & p_1^2(A_9 + 2A_8p_0 + 3A_7p_0^2 + 4A_6p_0^3 + 5A_5p_0^4 + 6A_4p_0^5 + 7A_3p_0^6 \\
 & + 8A_2p_0^7 + 9A_1p_0^8 + \frac{3A_7p_1^2}{4} + 3A_6p_0p_1^2 + \frac{15}{2}A_5p_0^2p_1^2 + 15A_4p_0^3p_1^2 + \frac{105}{4}A_3p_0^4p_1^2 \\
 & + 43A_2p_0^5p_1^2 + 63A_1p_0^6p_1^2 + \frac{5}{8}A_5p_1^4 + \frac{15}{4}A_4p_0p_1^4 + \frac{105}{8}A_3p_0^2p_1^4 + 35A_2p_0^3p_1^4 \\
 & + \frac{315}{4}A_1p_0^4p_1^4 + \frac{35}{64}A_3p_1^6 + \frac{35}{8}A_2p_0p_1^6 + \frac{315}{6}A_1p_0^2p_1^6 + \frac{63}{128}A_1p_1^8 - p_1\Omega)^2 \\
 & (-c_p\Omega)^2 = (P\Omega^2)^2
 \end{aligned}
 \tag{37}$$

$$\begin{aligned}
 T_d &= \frac{|P \cos(\Omega\tau) + p_1 \cos(\Omega\tau + \theta)|}{|P \cos(\Omega\tau)|} \\
 &= \frac{\sqrt{p_1^2 + P^2 + 2Pp_1 \cos(\theta)}}{P}
 \end{aligned}
 \tag{38}$$

Selecting the parameters in Table 2 and using Eq. (38) to obtain the vibration transmissibility of the CQZSVI in the three cases shown in Fig. 8 under the same linear stiffness. With the same rated load of 3 kg, the CQZSVIs constructed by the NMSM are compared with the QZSVIs obtained by the linear and the nonlinear stiffness compensation methods. The transmissibility comparison results are shown in Fig. 10 and Table 1. In Fig. 10a, the circles represent the transmissibility obtained by the fourth-order Runge–Kutta method based on Eq. (30) without polynomial approximation, and the solid lines represent the results obtained by Eq. (38). The attractors and

corresponding attraction domain of the CQZSVIs at their natural frequencies are shown in Fig. 11.

It can be seen from Fig. 10a that the numerical results obtained by Eq. (30) fit well with the theoretical results obtained by Eq. (38), denoting that the results of Eq. (38) are correct and can represent the vibration transmissibility property of the CQZSVI. Using Eq. (38) to analyze the vibration transmissibility of the CQZSVI will take much less time and is more efficient than using numerical methods. Under the same linear stiffness, the natural frequency of the CQZSVI obtained by the NMSM is obviously lower than that of the concave structure without stiffness compensation (the case of $\delta_1 = \delta_2 = 0$ in Fig. 10a). In these three different configurations as shown in Fig. 10a, when $\delta_1 > \delta_2$, the natural frequency is the largest, and the isolation frequency band is relatively narrow. When $\delta_1 = \delta_2 \neq 0$, the isolator possesses the smallest natural frequency as well as the widest vibration isolation frequency band. It should be noted that each of these three vibration isolators obtained by the NMSM has only one attractor in the resonant region, corresponding to a stable period-1 motion, as shown in Fig. 11. The x-axis represents their displacement ranges. Hence, the coexistence of multiple solutions has been eliminated, resulting in that no

Fig. 10 The vibration transmissibility of the isolators designed by the NMSM, **a** the transmissibility curves and enlarged diagram with different configurations; the comparison results of vibration transmissibility with **b** $\delta_1 > \delta_2$, **c** $\delta_1 < \delta_2$ and **d** $\delta_1 = \delta_2 \neq 0$

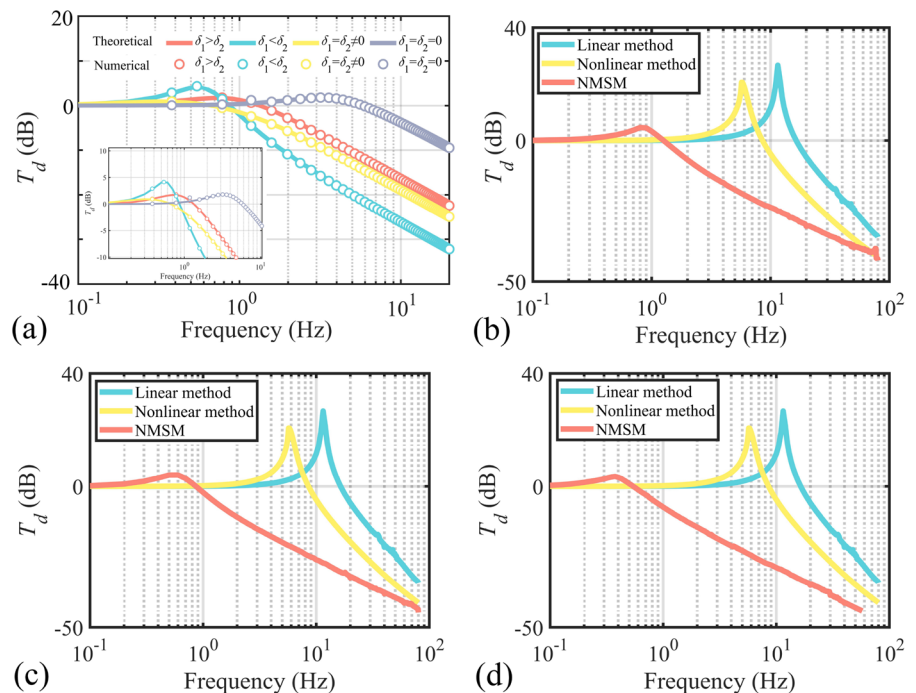


Table 1 The comparison results of the vibration isolators obtained by different methods

Type	Maximum T_d (dB)	Natural frequency (Hz)	Start-up frequency of vibration isolation (Hz)	T_d (dB) at 5 Hz	Rated load (kg)
$\delta_1 > \delta_2$	4.6104	0.8	1.13	- 17.38	3
$\delta_1 < \delta_2$	4.0713	0.6	0.85	- 19.78	3
$\delta_1 = \delta_2 \neq 0$	3.2533	0.4	0.57	- 22.71	3
Linear method	26.7196	11.5	16.5	1.81	3
Nonlinear method	20.6705	5.7	8.5	9.81	3

curve bending in the vicinity of the natural frequency in Fig. 10a. It denotes that the NMSM successfully suppresses stiffness hardening which causes coexistence of multiple solutions and curve bending.

Table 1 shows that considering the response amplitude, the peak of the transmissibility is relatively large when $\delta_1 < \delta_2$, while the smallest one occurs as $\delta_1 = \delta_2 \neq 0$. Within the vibration isolation region, the transmissibility of the condition $\delta_1 < \delta_2$ obviously lower than that of the other configurations, indicating the optimal vibration isolation performance. According to the above results, under the same linear stiffness, the configuration $\delta_1 < \delta_2$ has a relatively low natural frequency and a better bearing capacity (its payload is 2 to 3 times heavier than that of the other configurations). Therefore, this configuration has the best comprehensive vibration isolation performance among the CQZSVIs designed by the NMSM.

From Table 1, it can be seen that when the rated load is 3 kg, the natural frequency of the CQZSVI is less than 1 Hz, which is much lower than that of the vibration isolators obtained by the nonlinear stiffness compensation method (5.7 Hz) and the linear stiffness compensation method (11.5 Hz), leading to the widest vibration isolation band. In addition, the peak of the transmissibility of the CQZSVI (about 4 dB) is considerably lower than that of the other two isolators (about 20 to 26 dB). In terms of the vibration isolation performance, the CQZSVI also has the lowest vibration transmissibility within 100 Hz. For instance, the transmissibility of the CQZSVI at 5 Hz is about - 17.38 dB to - 22.71 dB, while the other two isolators are about 1.81 dB and 9.81 dB. Hence, the NMSM significantly weakens the stiffness hardening phenomenon compared with the other two methods,

leading to better ultra-low-frequency vibration isolation performance of the isolators.

5 Vibration experimentations

Based on the analysis of the statics property and the ultra-low-frequency vibration isolation performance of the CQZSVI, the optimal comprehensive performance is generated when the system parameters satisfy the situation $\delta_1 < \delta_2$. Hence, a prototype with the parameters satisfying $\delta_1 < \delta_2$ is fabricated to verify the correctness of the above theoretical results. The parameters used to fabricate the prototype are shown in Table 2. The parameters of the NS are shown in Table 3. The systems used to test the restoring force of the NS and that of the CQZSVI are shown in Fig. 12. The data of the statics experiments are shown in Fig. 13. The parameters of the NS in finite element are set as the elastic modulus 115.8 GPa, Poisson's ratio 0.29, and the mass density 7930 kg/m³. Each point of the experimental restoring forces in Fig. 13a, c is the average value of more than 300 practical data. The practical stiffness shown in Fig. 13b, d is obtained by calculating the first-order derivative of the restoring force with respect to the displacement. The QZS region is marked by the gray rectangle.

In Fig. 12, the actuator (PDS-500, TMAi, China) is used to exert displacement to the NS, and transmits the displacement data to the data collection system simultaneously. The force gauge (SH-III, NSCING ES, China) moving with the actuator connects the actuator with the NS, and collects the data of the restoring force of the NS. Then, the data are transmitted to the data collection system. Two linear bearings are used to reduce sliding friction during testing. The

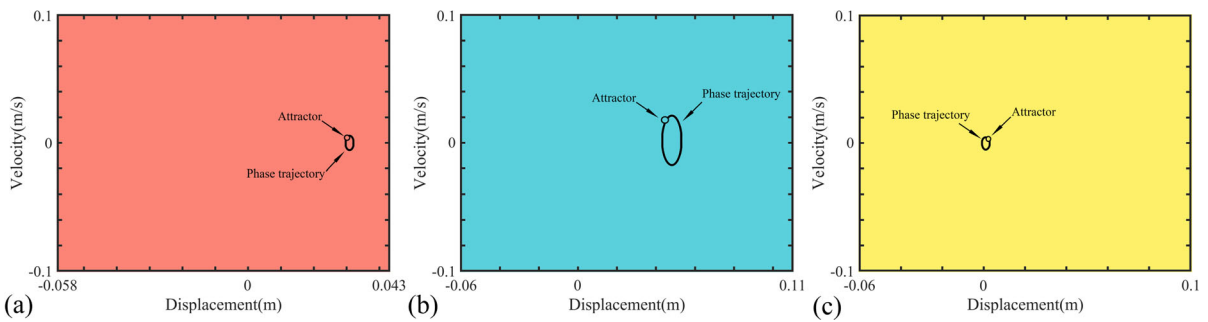


Fig. 11 The attractors and corresponding attraction domains at the natural frequency of **a** 0.8 Hz with $\delta_1 > \delta_2$, **b** 0.6 Hz with $\delta_1 < \delta_2$ and **c** 0.4 Hz with $\delta_1 = \delta_2 \neq 0$

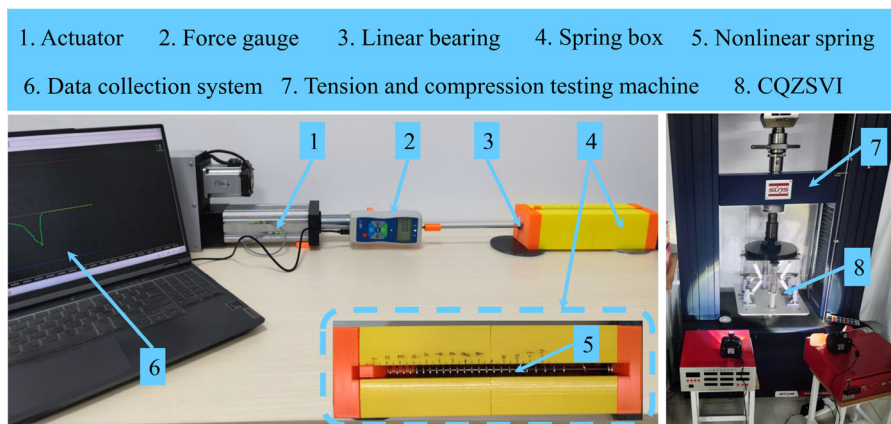


Fig. 12 The systems used to test the restoring force of the NS and the CQZSVI

NS is placed in the spring box to prevent bulking during compression. The equipment used to test the restoring force of the CQZSVI is a tension and compression testing machine (UTM5105SLXY, SUNS, China), which can exert accurate displacement to the vibration isolator.

Figure 13 exhibits that the experiment results are in good agreement with the theoretical results and finite element results, proving the validation of the NMSM and the correctness of the analytical expressions of the NS and the CQZSVI. As shown in Fig. 13, the displacement into the nonlinear region of the NS is the same as the displacement into the QZS region of the CQZSVI. This displacement calculated by Eq. (29) is about 0.07597 m, which is approximate the same as the results in Fig. 13. From Fig. 13a, b, the nonlinear restoring force and the variable stiffness property of the NS are radically demonstrated by the practical data. Figure 13e shows that in the linear

region, none of the coil of the NS is closed (subgraph I), the first coil is closed at χ_1 (subgraph II), and most of the coils are closed in the nonlinear region (subgraph III). The results in Fig. 13c, d clearly exhibit the broad QZS region and extremely weak stiffness hardening of the CQZSVI. After entering the QZS region, the restoring force and stiffness of the CQZSVI remain nearly constant. A video record is in the supplementary material to demonstrate the approximately invariable restoring force of the CQZSVI in the QZS region.

The vibration experiment system of the CQZSVI is shown in Fig. 14.

As shown in Fig. 14a, a vibration test bench is used to exert external excitation to the CQZSVI. The excitation signal is generated by a vibration controller (VT-9008, ECON, China), and transmitted to the vibration test bench through the power amplifier. The excitation signal and the vibration response signal are

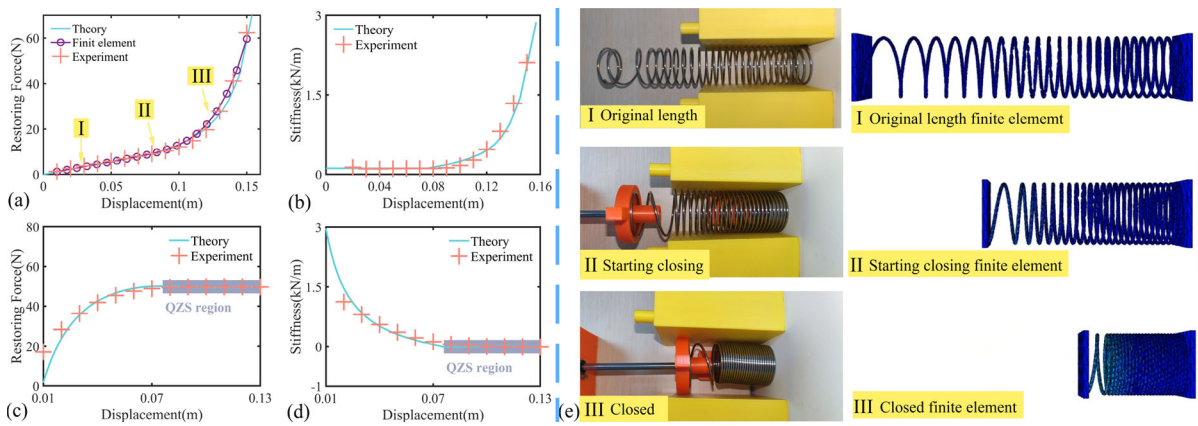


Fig. 13 The experiment results of the NS and the CQZSVI, **a** the practical restoring force of the NS, **b** the stiffness of the NS, **c** the practical restoring force of the CQZSVI, **d** the stiffness

of the CQZSVI, **e** different states of the NS in reality and in the finite element model

gathered by a signal collector (INV3062, COINV, China) through two acceleration sensors (1A314E, DONGHUA, China). The prototype of the CQZSVI designed by the NMSM is shown in Fig. 14b. Most parts of the prototype are made of aluminum alloy to reduce the weight. To ensure the symmetry of the CQZSVI, two NSs and four linear springs are installed. Deep groove ball bearings are added in the joints of the prototype to minimize the influence of sliding friction on the vibration response.

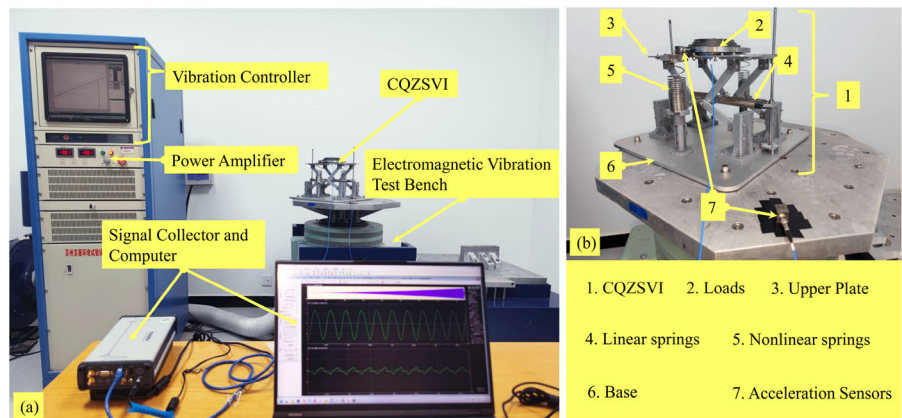
To prepare for sweep-frequency vibration experiments, the damping ratio was tested by the free vibration attenuation method, and verified by the half-power bandwidth method. The time history diagram of free vibration and the practical vibration transmissibility under external excitation with 6 mm amplitude are shown in Fig. 15. The damping ratio obtained by the free vibration attenuation method is about 0.1243. Based on the practical vibration transmissibility curve,

the result calculated by the half-power bandwidth method is about 0.1282. The two results are very close, which proves the correctness of the damping ratio and the feasibility for using a viscous damping model in Eq. (30).

Sweep-frequency vibration experiments with different amplitude are conducted. The frequency interval of the experiments is from 0.2 Hz to 4 Hz. The duration of each sweep-frequency experiment is 200 s that the sweep speed is slow enough for the CQZSVI to reach its steady state. The sampling frequency is 1024 points per second. The results of the sweep-frequency vibration experiments are shown in Fig. 16. The corresponding time history diagrams are shown in Fig. 17.

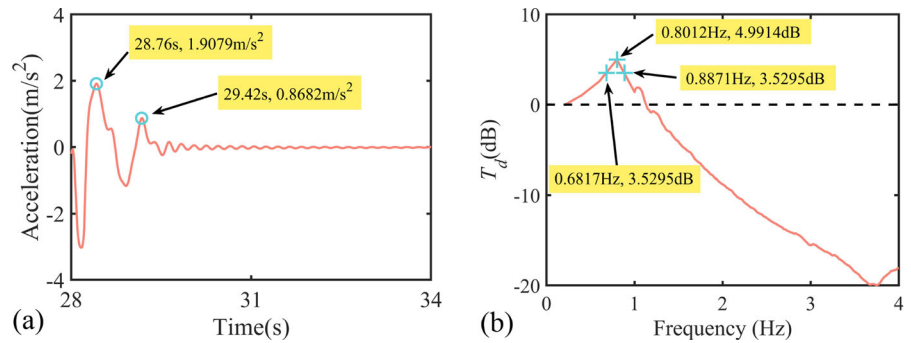
In Fig. 16, the effective vibration isolation regions are highlighted with yellow, and the initial frequencies of the effective vibration isolation regions are written on the diagrams and marked by the black dot-dash

Fig. 14 The vibration experiment system of the CQZSVI



- 1. CQZSVI
- 2. Loads
- 3. Upper Plate
- 4. Linear springs
- 5. Nonlinear springs
- 6. Base
- 7. Acceleration Sensors

Fig. 15 The data used for testing the damping ratio, **a** the results of free vibration, and **b** the practical vibration transmissibility under external excitation with 6 mm amplitude

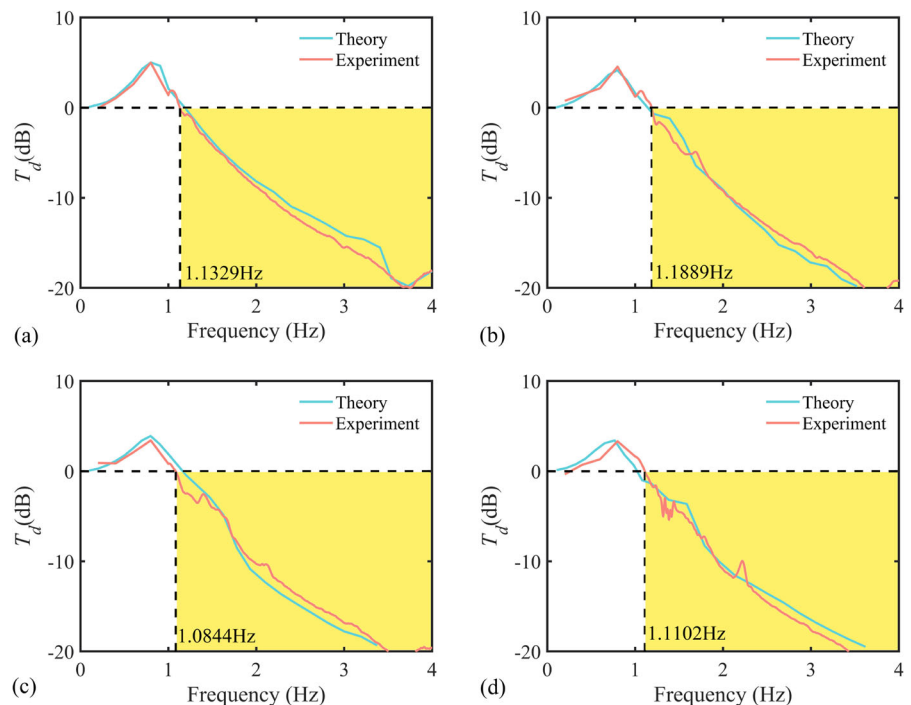


line. Figure 16 demonstrates that the experimental results fit well with the theoretical results, which verifies the correctness of the NMSM as well as that of the theoretical analysis of the CQZSVI. The unsmooth fluctuation on these curves is attributed to sub-resonance phenomena but does not affect the correctness of the theoretical analysis. The natural frequency in these diagrams is about 0.8 Hz. The transmissibility is about -15 dB at 3 Hz and is about -20 dB at 3.5 Hz, exhibiting the splendid ultra-low-frequency vibration isolation performance of CQZSVI. Further, the natural frequency and the initial frequency of the vibration isolation region are approximately unaffected by the increase in the excitation amplitude, demonstrating an extremely low dynamic stiffness of

the CQZSVI as well as the broad QZS region. The results shown in Fig. 16 radically exhibit the excellent inhibition of the NMSM for stiffness hardening.

From the left side of Fig. 17, the response at the upper plate is approximately the same as the excitation at the basement, indicating the entrance of the effective vibration isolation region of the CQZSVI. The right side of Fig. 17 clearly demonstrates that the displacement excitation exerted at the base has been considerably attenuated by the CQZSVI, resulting in that the response at 3 Hz is considerably smaller than the excitation. The results in Fig. 17 prove the excellent ultra-low-frequency vibration isolation performance of the CQZSVI.

Fig. 16 The results of the sweep-frequency experiments, **a** the amplitude is 6 mm, **b** the amplitude is 7 mm, **c** the amplitude is 8 mm, and **d** the amplitude is 9 mm



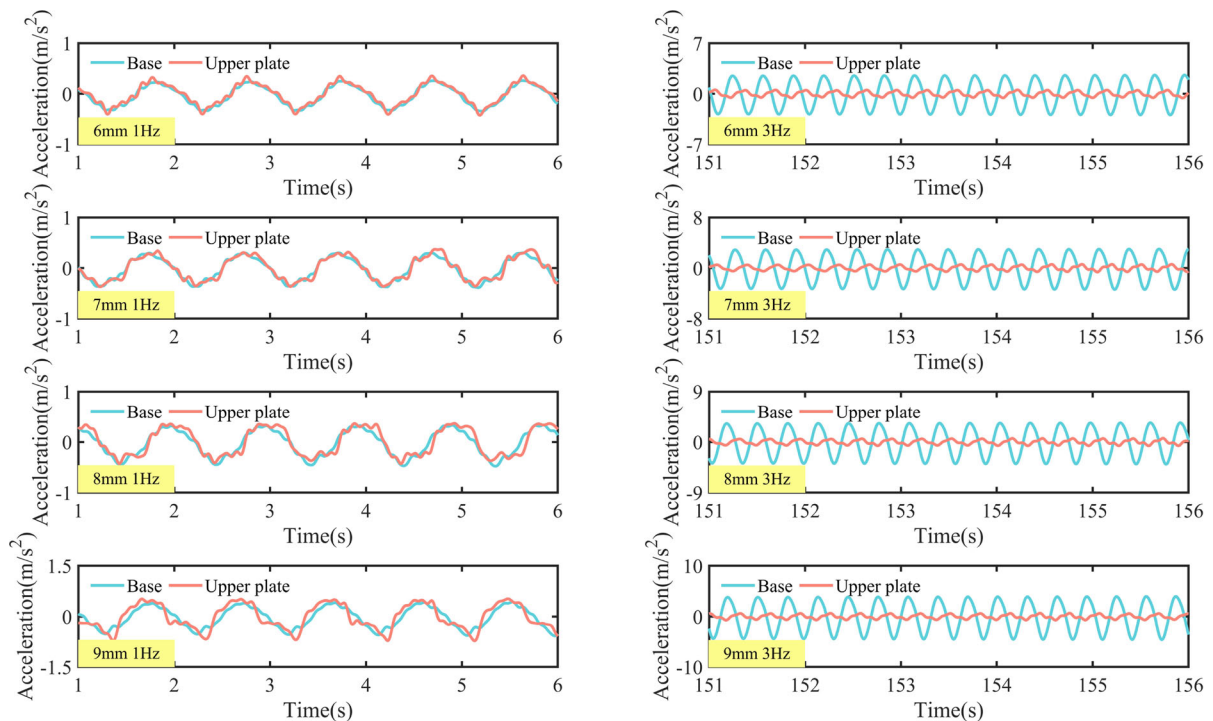


Fig. 17 The time history diagrams of the sweep-frequency vibration experiments with different excitation amplitudes at 1 Hz and 3 Hz

6 Conclusions

The NMSM is proposed to inhibit the phenomenon of stiffness hardening to break through the bottleneck of the development of QZSVIs. The mechanism and origination of the NMSM are clarified and its applicable condition is determined. The function of the equivalent stiffness of the NS is established with Heaviside function. A concave metastructure with multiple stiffness characteristics is constructed. To verify the effectiveness of the NMSM, different NSs are designed and are coupled with the concave metastructure to construct CQZSVIs. The theoretical analysis and the vibration experiments are conducted to investigate the inhibition of stiffness hardening by the NMSM and the ultra-low-frequency vibration isolation performance of the CQZSVI. Conclusions are summarized as follows.

The NMSM can significantly inhibit stiffness hardening phenomena through constructing the NS whose stiffness characteristics has a mirror-image relationship with the specific negative stiffness. The applicable condition of the NMSM requires the

changing rate of the targeted negative stiffness with respect to the displacement smaller than or equal to zero when the stiffness is less than zero. The increase in the number of the coil of the NS can enhance the inhibitory for stiffness hardening.

All of the CQZSVIs constructed by the NMSM has excellent ultra-low-frequency vibration isolation performance. Their natural frequencies are lower than 1 Hz considerably lower than that of the QZSVIs constructed by the linear compensation method or the nonlinear compensation method, demonstrating broad vibration isolation regions. Among these CQZSVIs, the one satisfying the condition $\delta_1 < \delta_2$ possesses the optimal vibration isolation performance.

The practical results of the restoring force and the stiffness of the NS reveal its nonlinear and variable stiffness characteristics, and verifies the correctness of its functional model. The practical restoring force and the stiffness of the prototype of the CQZSVI exhibit an obvious QZS region where the restoring force remains approximately constant and the stiffness is almost invariable and close to zero. The prototype of the CQZSVI has a natural frequency of about 0.8 Hz and a

broad effective vibration isolation region starting from about 1.1 Hz. Its transmissibility is about -15 dB at 3 Hz and is about -20 dB at 3.5 Hz, exhibiting splendid ultra-low-frequency vibration isolation performance.

The NMSM successfully weakens the stiffness hardening phenomenon, significantly broadens the vibration isolation frequency band, and provides a new approach for the construction of QZSVIs. The applicable condition of the NMSM is limited only by the changing rate of the negative stiffness curve, leading to that the size restriction of the NS can be flexibly designed according to the demand obtaining an extensive application prospect.

Acknowledgements This work was supported by the National Natural Science Foundation of China [Grant Numbers 12072203, 12102274, U23A2068], the Central Guidance on Local Science and Technology Development Fund of Hebei Province [Grant Number 226Z4901G], Top-notch Young Talent Program of Hebei Province Education Department of China [Grant Number BJK2023037], the Natural Science Foundation of Hebei Province of China [Grant Number A2023210064, A2022210005], and the Graduate Innovation Foundation of Hebei Province [Grant Number YC202440].

Author contributions Minghao Wang: Conceptualization, methodology, software, formal analysis, investigation, writing—original draft, visualization, supervision, funding acquisition. Ruilan Tian: Validation, resources, data curation, writing—review and editing, supervision project administration, Funding acquisition. Xiaolong Zhang: Writing—review and editing, validation, resources, supervision, funding acquisition. Shen Li: Investigation, methodology. Qiubao Wang: Writing—review and editing.

Data availability The datasets generated and analyzed during the current study are available from the corresponding author on reasonable request.

Declarations

Conflict of interest The authors declare that they have no conflict of interest.

Appendix A

See Tables 2 and 3.

Table 2 The parameters for different stiffness characteristics used for validate NMSM

Relationship	Parameters	Value
$\delta_1 > \delta_2$	k_0	605 N/m
	R_1	0.1 m
	R_2	0.12 m
	l_1	0.22 m
	l_2	0.21 m
	h	0.18 m
	h_2	0.065 m
	N	30
	δ_1	0.02 m
	δ_2	-0.03 m
$\delta_1 < \delta_2$	R_1	0.12 m
	R_2	0.1 m
	l_1	0.21 m
	l_2	0.22 m
	h	0.21 m
	h_2	0.065 m
	N	30
	δ_1	-0.03 m
	δ_2	0.02 m
	$\delta_1 = \delta_2 \neq 0$	R_1
R_2		0.1 m
l_1		0.24 m
l_2		0.22 m
h		0.18 m
h_2		0.065 m
N		30
δ_1		0.02 m
δ_2		0.02 m
$\delta_1 = \delta_2 = 0$		R_1
	R_2	0.11 m
	l_1	0.22 m
	l_2	0.22 m
	h	0.08 m
	h_2	0.065 m
	N	30
	δ_1	0 m
δ_2	0 m	

Table 3 The parameters of the NS

Parameter	Value
Material	SUS304-WPB
Stiffness	2951.6 N/m
d	2 mm
D	36.1 mm
N	25
κ_{11}	5 mm
κ_{12}	5.1 mm
κ_{13}	5.1 mm
κ_{14}	5.2 mm
κ_{15}	5.2 mm
κ_{16}	5.3 mm
κ_{17}	5.4 mm
κ_{18}	5.5 mm
κ_{19}	5.6 mm
κ_{110}	5.7 mm
κ_{111}	5.9 mm
κ_{112}	6.1 mm
κ_{113}	6.3 mm
κ_{114}	6.5 mm
κ_{115}	6.8 mm
κ_{116}	7.1 mm
κ_{117}	7.5 mm
κ_{118}	8 mm
κ_{119}	8.6 mm
κ_{120}	9.4 mm
κ_{121}	10.4 mm
κ_{122}	11.7 mm
κ_{123}	13.6 mm
κ_{124}	17.4 mm
κ_{125}	29.5 mm

References

- Zhao, T.Y., Yan, G., Qi, W.H., Lu, J.J., Zhang, W.M.: Magnetically modulated tetrahedral structure for low frequency vibration isolation with adjustable load capacity. *Mech. Syst. Signal Process.* **251**, 108335 (2023)
- Ling, P., Miao, L.L., Ye, B.L., You, J., Zhang, W.M., Yan, B.: Ultra-low frequency vibration isolation of a novel click-beetle-inspired structure with large quasi-zero stiffness region. *J. Sound Vib.* **558**, 117756 (2023)
- Kocak, K., Yilmaz, C.: Design of a compliant lever-type passive vibration isolator with quasi-zero-stiffness mechanism. *J. Sound Vib.* **558**, 117758 (2023)
- Zhou, S.H., Xu, P.Z., Hou, B.W., Ren, Z.H.: Dynamic characteristics analysis of bilayer bio-inspired X-shaped vibration isolation structure. *Int. J. Nonlinear Mech.* **154**, 104447 (2023)
- Ma, Z.Z., Zhou, R.P., Yang, Q.C., Lee, H.P., Chai, K.: A semi-active electromagnetic quasi-zero-stiffness vibration isolator. *Int. J. Mech. Sci.* **252**, 108357 (2023)
- Lane, S.A., Murphey, T.W., Zatman, M.: Overview of the innovative space-based radar antenna technology program. *J. Spacecr. Rocket.* **48**, 135–145 (2011)
- Zhao, F., Cao, S.Q., Luo, Q.T., Ji, J.C.: Enhanced design of the quasi-zero stiffness vibration isolator with three pairs of oblique springs: theory and experiment. *J. Vib. Control* **29**, 2049–2063 (2023)
- Wang, Q., Zhou, J.X., Wang, K., Gao, J.H., Lin, Q.D., Chang, Y.P., Xu, D.L., Wen, G.L.: Dual-function quasi-zero-stiffness dynamic vibration absorber: low-frequency vibration mitigation and energy harvesting. *Appl. Math. Model.* **116**, 636–654 (2023)
- Zhou, J.X., Xiao, Q.Y., Xu, D.L., Ouyang, H.J., Li, Y.L.: A novel quasi-zero-stiffness strut and its applications in six-degree-of-freedom vibration isolation platform. *J. Sound Vib.* **394**, 59–74 (2017)
- Li, Y., Chang, Y.P., Zhou, J.X., Wang, K.: Dual quasi-zero-stiffness dynamic vibration absorbers for double-low-frequency vibration suppression. *Int. J. Mech. Sci.* **264**, 108852 (2024)
- Ji, L.W., Luo, Y.J., Zhang, Y.H., Xie, S.L., Xu, M.H.: A creative wide-frequency and large-amplitude vibration isolator design method based on magnetic negative stiffness and displacement amplification mechanism. *J. Sound Vib.* **572**, 118185 (2024)
- Yu, C.Y., Jiang, Q.B., Fu, Q.D., Yu, K.F., Zhang, J.R., Zhang, N.: The X-shaped structure with nonlinear positive stiffness compensation for low-frequency vibration isolation. *Int. J. Mech. Sci.* **259**, 108598 (2023)
- Bian, J., Jing, X.J.: Analysis and design of a novel and compact X-structured vibration isolation mount (X-Mount) with wider quasi-zero stiffness range. *Nonlinear Dyn.* **101**, 2195–2222 (2020)
- Chen, Z.H., Yue, X.K., Jing, X.J., Dai, H.H.: Spider-inspired anti-impact hydraulics-based structure for on-orbit capture. *Nonlinear Dyn.* **111**, 14925–14956 (2023)
- Banerjee, P., Dalela, S., Balaji, P.S., Murugan, S., Kumaraswamidhas, L.A.: Simultaneous vibration isolation and energy harvesting using quasi-zero-stiffness-based metastructure. *Acta Mech.* **234**, 3337–3359 (2023)
- Lin, Q.D., Zhou, J.X., Wang, K., Xu, D.L., Wen, G.L., Wang, Q.: Three-dimensional quasi-zero-stiffness metamaterial for low-frequency and wide complete band gap. *Compos. Struct.* **307**, 116656 (2023)
- Liu, J., Wang, Y.H., Yang, S.Q., Sun, T.S., Yang, M., Niu, W.D.: Customized quasi-zero-stiffness metamaterials for ultra-low frequency broadband vibration isolation. *Int. J. Mech. Sci.* **269**, 108958 (2024)
- Carrella, A., Brennan, M.J., Waters, T.P.: Static analysis of a passive vibration isolator with quasi-zero-stiffness characteristic. *J. Sound Vib.* **301**, 678–689 (2007)

19. Hao, Z.F., Cao, Q.J.: The isolation characteristics of an archetypal dynamical model with stable-quasi-zero-stiffness. *J. Sound Vib.* **340**, 61–79 (2015)
20. Yang, T., Cao, Q.J., Li, Q.Q., Qiu, H.Q.: A multi-directional multi-stable device: modeling, experiment verification and applications. *Mech. Syst. Signal Process.* **146**, 106986 (2021)
21. Fang, S.T., Chen, K.Y., Zhao, B., Lai, Z.H., Zhou, S.X., Liao, W.H.: Simultaneous broadband vibration isolation and energy harvesting at low frequencies with quasi-zero stiffness and nonlinear monostability. *J. Sound Vib.* **553**, 117684 (2023)
22. Li, Z.Y., Wang, K., Chen, T.T., Cheng, L., Xu, D.L., Zhou, J.X.: Temperature controlled quasi-zero-stiffness metamaterial beam for broad-range low-frequency band tuning. *Int. J. Mech. Sci.* **259**, 108593 (2023)
23. Deng, L., Sun, S.S., Wu, Q.H., Gong, N., Yang, J., Zhang, S.W., Du, H.P., Li, W.H.: A new magnetorheological quasi-zero stiffness vibration isolation system with large zero stiffness range and highly stable characteristics. *Nonlinear Dyn.* **111**, 18631–18653 (2023)
24. Zhou, S.H., Hou, B.W., Zheng, L.S., Xu, P.Z., Yu, T.Z., Ren, Z.H.: Nonlinear property and dynamic stability analysis of a novel bio-inspired vibration isolation–absorption structure. *Nonlinear Dyn.* **112**, 887–902 (2024)
25. Pu, H.Y., Liu, J., Wang, M., Ding, J.H., Sun, Y., Peng, Y., Luo, J.: Bio-inspired quasi-zero stiffness vibration isolator with quasilinear negative stiffness in full stroke. *J. Sound Vib.* **574**, 118240 (2024)
26. Gatti, G., Svelto, C.: Performance of a vibration isolator with sigmoidal force-deflection curve. *J. Vib. Control* **29**, 5713–5724 (2023)
27. Jiang, T.J., Han, Q., Li, C.L.: Design and compression-induced bandgap evolution of novel polygonal negative stiffness metamaterials. *Int. J. Mech. Sci.* **261**, 108658 (2024)
28. Ma, H.Y., Wang, K., Zhao, H.F., Zhao, C., Xue, J., Liang, C., Yan, B.: Harnessing chiral buckling structure to design tunable local resonance metamaterial for low-frequency vibration isolation. *J. Sound Vib.* **565**, 117905 (2023)
29. Zhang, Q., Guo, D.K., Hu, G.K.: Tailored mechanical metamaterials with programmable quasi-zero-stiffness features for full-band vibration isolation. *Adv. Funct. Mater.* **31**, 2101428 (2021)
30. Yan, G., Wu, Z.Y., Wei, X.S., Wang, S., Zou, H.X., Zhao, L.C., Qi, W.H., Zhang, W.M.: Nonlinear compensation method for quasi-zero stiffness vibration isolation. *J. Sound Vib.* **523**, 116743 (2022)
31. Yan, G., Lu, J.J., Qi, W.H., Liu, F.R., Yan, H., Zhao, L.C., Wu, Z.Y., Zhang, W.M.: Linear and nonlinear stiffness compensation for low-frequency vibration isolation: a comparative study. *Nonlinear Dyn.* **112**, 5955–5973 (2024)
32. Yu, N., Yang, K., Wu, Z.M., Zhang, W.M., Yan, B.: Low-frequency vibration absorption of magnetic quasi-zero-stiffness structures with lever mechanism. *Int. J. Mech. Sci.* **267**, 108973 (2024)
33. Ye, L.Z., Liang, C., Liu, Y.P., Li, D.S., Liu, Z.G.: Performance analysis and test of a novel eddy-current braking & heating system for electric bus. *Energ. Convers. Manag.* **183**, 440–449 (2019)
34. Zhang, X.L., Hao, H.N., Tian, R.L., Xue, Q., Guan, H.T., Yang, X.W.: Quasi-static compression and dynamic crushing behaviors of novel hybrid re-entrant auxetic metamaterials with enhanced energy-absorption. *Compos. Struct.* **288**, 115399 (2022)
35. Hou, S., Wei, J.Z.: A quasi-zero stiffness mechanism with monolithic flexible beams for low-frequency vibration isolation. *Int. J. Mech. Sci.* **210**, 111154 (2024)
36. Lu, H.J., Meng, L.X., Wang, J.K., Wang, Y., Zhang, L.Z.: Design and performance study of metamaterial with quasi-zero stiffness characteristics based on human body structure. *J. Vib. Eng. Technol.* **12**, 633–648 (2024)
37. Xiao, L., Sun, X., Cheng, L., Yu, X.: A 3D-printed quasi-zero-stiffness isolator for low-frequency vibration isolation: Modelling and experiments. *J. Sound Vib.* **577**, 118308 (2024)
38. Tian, R.L., Guan, H.T., Lu, X.H., Zhang, X.L., Hao, H.N., Feng, W.J., Zhang, G.L.: Dynamic crushing behavior and energy absorption of hybrid auxetic metamaterial inspired by Islamic motif art. *Appl. Math. Mech.* **44**, 345–362 (2023)
39. Cao, Q.J., Wiercigroch, M., Pavlovskaja, E.E., Thompson, G.M.T., Grebogi, C.: Piecewise linear approach to an archetypal oscillator for smooth and discontinuous dynamics. *Phil. Trans. R. Soc. A* **366**, 635–652 (2008)
40. Wang, M.H., Chen, E.L., Tian, R.L., Wang, C.Y.: The nonlinear dynamics characteristics and snap-through of an SD oscillator with nonlinear fractional damping. *Fractal. Fract.* **6**, 493 (2022)
41. Zhang, Z.W., Tian, R.L., Zhang, X.L., Wei, F.Y., Yang, X.W.: A novel butterfly-shaped auxetic structure with negative Poisson's ratio and enhanced stiffness. *J. Mater. Sci.* **56**, 141396–141456 (2021)
42. Tian, R.L., Wang, M.H., Zhang, Y.S., Jing, X.J., Zhang, X.L.: A concave X-shaped structure supported by variable pitch springs for low-frequency vibration isolation. *Mech. Syst. Signal Process.* **218**, 111587 (2024)
43. Gatti, G., Svelto, C.: Exploiting nonlinearity for the design of linear oscillators: Application to an inherently strong nonlinear X-shaped-spring suspension. *Mech. Syst. Signal Process.* **197**, 110362 (2023)
44. Anastasio, D., Marchesiello, S., Svelto, C., Gatti, G.: Experimental characterization of a nonlinear mechanical oscillator with softening behaviour for large displacements. *Nonlinear Dyn.* **112**, 7817–7830 (2024)

Publisher's Note Springer Nature remains neutral with regard to jurisdictional claims in published maps and institutional affiliations.

Springer Nature or its licensor (e.g. a society or other partner) holds exclusive rights to this article under a publishing agreement with the author(s) or other rightsholder(s); author self-archiving of the accepted manuscript version of this article is solely governed by the terms of such publishing agreement and applicable law.